Mesoporous nickel-alumina catalysts derived from MIL-53(Al) metal-organic framework: A new promising path for synthesizing CO2 methanation catalysts

Leila Karam, Maria C Bacariza, José M Lopes, Carlos Henriques, Julien Reboul, Nissrine El Hassan, Pascale Massiani

Mesoporous nickel-alumina catalysts derived from MIL-53(Al) metal-organic framework: A new promising path for synthesizing CO_2 methanation catalysts

Leila Karam[a,b*], Maria C. Bacariza[c], José M. Lopes[c], Carlos Henriques[c], Julien Reboul[a*], Nissrine El Hassan[b], Pascale Massiani[a]

[a] Sorbonne Université, UPMC, Laboratoire de Réactivité de Surface, UMR CNRS 7197, 4 Place Jussieu, Paris, France.

[b] University of Balamand, Department of Chemical Engineering, P.O. Box 33, Amioun El Koura, Lebanon.

[c] Centro de Química Estrutural, Instituto Superior Técnico, Universidade de Lisboa, Av. Rovisco Pais, 1049-001 Lisboa, Portugal.

*Corresponding authors: julien.reboul@sorbonne-universite.fr and leila.e.karam@gmail.com

Abstract

A new synthesis route for the preparation of highly efficient and stable porous Ni-based alumina catalysts for CO_2 methanation is presented. It is based on the use of MIL-53(Al), an Al-containing metal-organic framework (MOF) with high surface area, as sacrificial support. A series of Ni-Al_2O_3 powder samples with Ni loadings ranging from 5 to 20 wt.% was thus obtained. Their properties were thoroughly characterized by a set of complementary techniques including N_2-sorption, X-ray diffraction (XRD), thermo-gravimetric analysis (TGA), CO_2 adsorption, temperature programmed reduction (H_2-TPR) and transmission electron microscopy (TEM). After nickel impregnation and thermal assisted organic ligands elimination, the resulting Ni-Al_2O_3 materials appear as interwoven alumina nanosheets in which Ni cations are intimately mixed forming $NiAl_2O_4$ spinel nanophases dispersed within amorphous alumina. This nanosheet morphology is preserved after the reduction of the Ni cations that leads to Ni^0-Al_2O_3 catalysts composed of homogeneously and highly dispersed Ni^0 nanoparticles, even at the highest 20 wt% Ni content. As a result, the activity in CO_2 methanation, evaluated between 250 to 450 °C under atmospheric pressure, using a constant gas hourly space velocity of 68900 h^{-1} and a molar reactant ratio H_2/CO_2 of 4, increased proportionally with respect to the Ni loading. On the most active catalyst, the selectivity to CH_4 was always excellent (between 96% and 100%) and the obtained CH_4 yield (~70% at 300 ºC) was about two times higher than on a commercial Ni-based Al_2O_3 catalyst containing 25 wt% of Ni. The catalytic performances were also better than those of the already reported porous catalysts Ni/USY, Ni/SBA-15 as well as a Ni-Al_2O_3 synthesized by a EISA one-pot procedure, tested under the same reaction conditions for comparison. In this work the utilization of MIL-53(Al) as starting material for the synthesis of Ni-Al_2O_3 catalysts was responsible for a peculiar improvement of the metallic dispersion due to the high surface area of this MOF and of the metal-support interaction likely due to the existence of remaining $NiAl_2O_4$ at the metal-support interface. Sintering and agglomeration (the main cause of deactivation) were therefore

limited, thus boosting the catalytic performance (activity, selectivity and stability). **Keywords:** CO_2 methanation; Nickel nanoparticles; MIL-53(Al); mesoporous Al_2O_3; metal-support interaction

1. Introduction

Power-to-gas strategies that foresee a more efficient use of renewable sources for the production of energy have been widely explored in the recent years [1–5]. One of the promising approaches consists in storing the electrical surplus issued from wind or solar technologies via a chemical route which involves reacting renewable H_2 (electrically produced by water splitting) with CO_2 (a greenhouse gas) to produce methane [2–4,6]. The obtained synthetic natural gas (SNG) can then be consumed directly as an energy feedstock or be used as an energy storage system (able to give back H_2). An advantage of this chemical storage system is that methane is safer than H_2 and distributable through the existing natural gas grid. Moreover, such process, leads to CO_2 emissions mitigation and to the management of the unpredictable renewable sources.

CO_2 methanation is thermodynamically the most favourable route for carbon dioxide hydrogenation [7]. To ensure high CH_4 selectivity, a medium temperature is needed (between 200 and 400 °C) to avoid side reactions, especially the reverse water gas shift reaction that occurs above 450°C and produces CO [8]. Nevertheless, CO_2 methanation is also a kinetically limited eight-electron process [9], therefore a very active catalyst is mandatory, at such low temperatures, to achieve acceptable rates of reductive hydrogenation of CO_2 into CH_4. Amongst the recent studies on CO_2 methanation catalysts, many have been dedicated to nickel (a transition metal) based on its promising activity, selectivity and comparatively low price compared to noble metals. Attempts were done to enhance the catalysts performances by playing on the nickel dispersion [9], increasing its interaction and/or electron transfer with the support [10], or introducing defect (anchoring) sites on the support [11]. Different types of supports were also tested, including porous/non-porous alumina (Al_2O_3) (which is robust, thermally stable, favourable surface properties), ceria (CeO_2) and zirconia (ZrO_2) (whose redox properties increases oxygen vacancies, it also has good thermal stability), hydrotalcites (owing to its capacity to reduce Ni species and to host high Ni amount with good dispersion), zeolites (some of them present chemically active nanostructures and space for sorption properties enhancement), MgO (owing to its basicity) and natural clays (they possess environmental compatibility, low cost, reusability, and operational simplicity) [12–15]. However, CO_2 conversions often remained unsatisfactory in the conditions applied and temperature increase did not provide any improvement because of affecting negatively the selectivity to methane and also the efficiency of the catalyst due to nickel sintering and formation of coke deposits. In order to limit such drawbacks, a positive effect of using a support with

regular porosity, high surface area and wide pore diameter was demonstrated [16,17]. Moreover, among the tested supports, alumina (mainly ɣ-Al_2O_3) was the most widely used due its easy access, developed surface area and known surface acid–base properties that contribute to CO_2 adsorption/activation [18].

Recently, we reported the preparation of very efficient mesoporous Ni/alumina catalysts prepared by one-pot able to resist the high temperatures imposed by thermodynamics during dry reforming of methane (DRM) reaction [19], whose conditions are much harsher than those for CO_2 methanation. These samples modified with different amount of magnesium booster showed indeed excellent performances in CO_2 methanation as well [20]. For further development in the alumina catalyst system, a more innovative synthesis route was adapted. This process consisted of using an aluminium-based Metal-Organic Frameworks (MOF) as sacrificial parent support capable of intimately mixing nickel and aluminium cations. MOF are indeed excellent candidates for this purpose due to their opened porosity and very high surface area (1000-3000 $m^2.g^{-1}$) that can help in dispersing and stabilizing guest metal cations in close proximity to the framework inorganic cornerstones. Noteworthy, the use of MOFs, which are hybrid materials built from a coordination of metal ions (clusters) with organic ligands (linkers), as catalyst supports under gas phase conditions is still in its infancy. Certain catalysts made of MOF hosting platinum, nickel or ruthenium metal nanophases were indeed recently reported [21] leading to performances that overcame those obtained on conventional oxide supports. Nevertheless, a drawback of MOFs is their well-known thermal instability due to linkers degradation at the temperatures at which catalytic reactions usually take place. Thus, an alternative is to use MOFs as a precursor, giving after linker degradation, a stable carbonaceous or purely inorganic material depending on the initial MOF composition and thermal treatment adopted. This route was recently applied to prepare Ru/ZrO_2 catalysts with highly dispersed Ru (nanoparticles size of 2-5 nm) [22] or to obtain Co-containing porous carbons in which sintering of the Co nanoparticles was prevented owing to their separation by the graphite-like carbon sheets [23]. We also recently used this approach to develop new performing porous Ni/alumina DRM catalyst containing 5 wt.% of Ni, [24,25] synthesized from MIL-53(Al), a MOF composed of aluminium hydroxyl chains connected to each other by terephthalate ligands [24]. This MOF was first impregnated with a nickel precursor solution to set the metal cations in proximity with the Al nods, then a calcination step was carried out to eliminate the organic linkers resulting in nickel aluminate nanophases homogeneously dispersed within an amorphous alumina. This mixed metal oxide phase is believed to be the key intermediate responsible for the remarkably high dispersion and stability of the nickel active phase formed after the final reduction step.

This MIL-53(Al)-derived route is extended in the present work to prepare a series of novel porous Ni-Al_2O_3 materials with increasing Ni contents (from 5 to 20 wt.%) and test them for the first time in CO_2 methanation. A complementary set of physicochemical techniques (XRF, XRD, N_2-sorption, TGA, CO_2 adsorption, H_2-TPR and HR-TEM) is used to identify the impact of the increasing Ni content on the structural, textural and surface properties of the materials. The nickel state, location and dispersion are also carefully analysed. Finally, the performances are tested in CO_2 methanation and discussed in view of the materials properties. For the sake of completion, the physicochemical characteristics and performances of the new MOF-derived materials are also compared to those of more conventional catalysts containing 15 wt.% Ni supported on ordered porous oxides (mesoporous Ni-alumina, microporous Ni/zeolite and mesoporous Ni/SBA-15) and to a commercial Ni-alumina catalyst containing a higher Ni loading (25 wt.%).

2. Experimental

2.1. Materials preparation

A parent MIL-53(Al) sample was synthesized according to a known procedure [26]. It consisted of mixing 1.21 g of $AlCl_3.6H_2O$ and 0.42 g of benzene-1,4-di-carboxylic acid with 3 ml water and 5 ml of dimethylformamide (DMF), then transferring the mixture into a 50 ml reactor and heating it in a microwave oven for 30 minutes at 125 °C under a power of 200 W. The resultant precipitate was recovered by centrifugation, washed six times in 10 mL DMF solution and in 10 mL deionized water to ensure full removal of unwanted residues (unreacted terephthalic acid, aluminium salt and solvents). After centrifugation, the white powder was dried for 24 h at 80 °C and heated in air at 220 °C for 72 h to obtain the activated (adsorbate free) sample, denoted **MIL-53**.

Nickel impregnation was then performed by adding dropwise a $Ni(NO_3)_2.6H_2O$ aqueous solution with a volume chosen similar to the MIL-53 pore volume (as determined from N_2-sorption, see below) and a nickel concentration corresponding to a Ni content (in the reduced catalyst) of either 5, 15 or 20 wt.%. These impregnated samples were dried at room temperature for 24 h, then treated in static air for 5 h at 500 °C (thin bed conditions, heating rate of 0.5 °C.min^{-1}) to decompose the organic linkers and obtain the series of calcined **Ni_x-$Al_2O_{3\text{-MIL-53}}$** materials (where x is the Ni wt.%). Below is a brief schematic illustrating the MOF based catalyst preparation (Scheme 1).

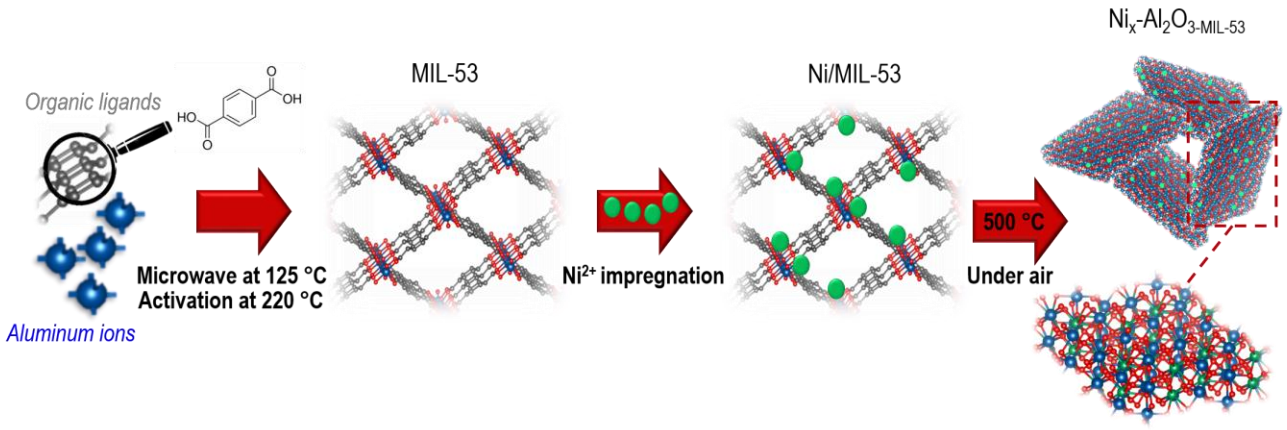

Scheme 1: Schematic summarizing the MOF-based preparation route of the Ni-alumina catalyst (Ni_x-$Al_2O_{3\text{-}MIL\text{-}53}$).

For comparison purposes, an ordered mesoporous **Ni_{15}-$Al_2O_{3\text{-}OP}$** material containing 15 wt.% of nickel was also synthetized, following our recently described evaporation induced self-assembly (EISA) one-pot method [19], and a commercial **Ni_{25}/γ-Al_2O_3** catalyst containing ~25 wt.% Ni (Evonik) was used. Moreover, two silica-based catalysts referred as **Ni_{15}/USY** and **Ni_{15}/SBA-15** were prepared by incipient wetness impregnation with 15 wt.% nickel of a Cs-USY zeolite (Si/Al_{global} ratio = 38) [27,28] and of a commercial SBA-15 [29], respectively. Part of each sample was submitted to reduction in a flow of 5%H_2/Ar (25 mL.min^{-1}) in the conditions of H_2-TPR measurement to prepare the reduced catalysts. The temperatures of reduction were chosen according to the H_2-TPR profiles (Fig. 5A) and were as follows; 650°C ($Ni^0{}_{15}$/SBA-15), 700°C ($Ni^0{}_{15}$/USY) and 800°C ($Ni^0{}_x$-$Al_2O_{3\text{-}MIL53}$, $Ni^0{}_{15}$-$Al_2O_{3\text{-}OP}$ and $Ni^0{}_{25}/\gamma$-Al_2O_3).

2.2. Materials characterization

X-Ray Fluorescence (XRF) carried out on a XEPOS spectrometer (Spectro Ametek) was used to measure and validate the Ni contents using a MicroPowder method and a calibration curve previously established from NiO and alumina mixtures with known chemical compositions.

Thermogravimetric (TGA) analyses were performed on a Setsys Evolution TGA (Setaram instruments). The samples were saturated with water prior experiment, then the temperature was raised from room temperature till 400 ºC (heating rate of 10 ºC/min) under air flow (30 mL/min). Water desorption, occurring in this temperature range and giving an endothermic peak as confirmed by DSC, was used to determine the h index indicative of the water affinity with the sample [27,30] and calculated as the ratio between the mass losses at ~150 ºC (weakly interacting water molecules) and ~ 400 ºC (strongly interacting water molecules).

Powder XRD patterns were obtained on a Bruker AXS Advance D8 diffractometer equipped with a 1D detector (SSD 160). The Cu Kα radiation was used and the equipment was operated at 40 kV and 40 mA. The scanning range was set from 5° to 80° (2θ), with a step size of 0.03º/2s. The Scherer equation was applied to evaluate the average size (D in nm) of crystal domains (NiO or $NiAl_2O_4$ before reduction and Ni^0 after reduction), expressed as $D=K\lambda/\beta\cos\theta$ where K=0.9 is a constant, λ is the wavelength of the incident X-ray beam, β is the full width at half maximum (FWHM) of the diffraction peaks, and θ corresponds to peak position usually taken in our study at 2θ = 45° for NiO or $NiAl_2O_4$, and 50.9° for Ni^0.

N_2 adsorption-desorption isotherms were recorded at -196 °C using a BELsorp-max (MicrotracBEL) apparatus. Each sample was firstly degassed under vacuum for 2 h at 250 °C (7 h at 200 °C for MIL-53(Al)), then placed at liquid nitrogen temperature afterwards the N_2-isotherm was plotted. Specific surface areas were calculated from the BET equation at relative pressures between 0.05 and 0.25. The corresponding single point pore volume was obtained from the sorption branch at a relative pressure of 0.99.

CO_2 isotherms were collected at 0 ºC on an Autosorb iQ equipment from Quantachrome. Before adsorption, the samples were degassed under vacuum at 90 ºC for 1 h and then at 350 ºC for 4 h. Experiments were run using the same conditions applied in previous works [27,31,32].

H_2-TPR studies were performed in a Micromeritics AutoChem II instrument. The samples (~100 mg) were first pre-treated at 250 °C under argon flow, then cooled down to room temperature, and reduction was carried out in a 5%H_2/Ar flow (25 $mL.min^{-1}$) with a temperature increase from room temperature to 900 °C (heating rate of 10 ºC/min). A TCD detector was used to quantify the hydrogen consumption. Before reaching it, the outlet gas was passed in a cold trap (CO_2 ice temperature) to remove the water molecules formed during reduction ($H_{2(g)}+NiO_{(s)}\rightarrow Ni^0_{(s)}+H_2O_{(g)}$).

High-resolution transmission electron microscopy (HRTEM) images were taken on a JEOL-JEM 200 electron microscope operating at 200 keV (LaB_6 gun). Before observations, the powders were suspended in ethanol for few minutes under ultrasound vibration, and then deposited on a copper grid coated with carbon membrane (microtomy). The "*Comptage de Particules*" software available at LRS was considered to estimate the average particle size of nickel (Ni^0) particles. To do so, around 500 particles present in the grains were taken into consideration where the channels are oriented parallel to the electron beam.

2.3. Catalytic tests

Catalytic tests were conducted in a fixed-bed reactor at atmospheric pressure. Prior to reaction, all samples (200 mg) were *in-situ* reduced under an 80%H_2/N_2 flow (250 mL.min^{-1}) at a heating rate of 5 ºC.min^{-1} from room temperature till a selected maximum temperature that was maintained for 1 h. This temperature was chosen from H_2-TPR profiles ~~as~~ to allow the complete nickel reduction species into metallic Ni^0. The value of the temperature was equal to 650 ºC for Ni_{15}/SBA-15, 700 °C for Ni_{15}/USY and 800 ºC for Ni_x-$Al_2O_{3\text{-MIL-53}}$, Ni_{15}-$Al_2O_{3\text{-OP}}$ and commercial Ni_{25}/γ-Al_2O_3. The reactants were next introduced into the reactor at a molar ratio of H_2:CO_2:N_2 = 36:9:10 (total flow of 287 mL.min^{-1}) and the CO_2 methanation reaction was performed stepwise, at temperatures ranging from 250 to 450 ºC. The global inlet volumetric flow rate, leading to a gas hourly space velocity (GHSV) of 68900 h^{-1}, was chosen based on previous studies which proved that these experimental conditions avoid external mass diffusion limitations.

Air Liquide supplied all gases, with purities ≥99.9990%. The reactor effluent was analysed using three Guardian® NG infrared detectors (Edinburgh Sensors) for CO_2, CH_4 and CO. The outlet flow was simultaneously measured to estimate the variation of the number of moles consecutive to the Sabatier reaction ($CO_2 + 4H_2 \rightarrow CH_4 + 2H_2O$) and take it into account in the determination of the catalytic performances expressed as CO_2 conversion ($X_{CO2} = mol_{CO2\text{-transformed}}/mol_{CO2\text{-inlet}}$) and selectivity to CH_4 ($S_{CH4} = mol_{CH4\text{-produced}}/mol_{CO2\text{-converted}}$). Carbon balances were systematically evaluated to verify the absence of by-products in the effluents where only CH_4 and CO were detected as products. In addition, turnover frequency numbers (TOF) were calculated using the equation: $TOF\ (s^{-1}) = X \cdot F_{Ae} \cdot Mw_{Ni}\ (1/W) \cdot (1/D_{Ni}).(1/X_{Ni})$, where X is the CO_2 conversion, F_{Ae} is the inlet molar flow of CO_2 ($mol_{CO2\ inlet}.min^{-1}$), W is the mass of catalyst ($g_{catalyst}$), D_{Ni} is the nickel dispersion and X_{Ni} is the nickel content ($g_{Ni}.g_{cat}^{-1}$) [33].

Finally, and with the aim of comparing the results of the most outstanding catalyst from this work with literature, average CO_2 reaction rates (r) were determined by Equation 1, with $F_{CO2.inlet}$ ($mol_{CO2}.s^{-1}$) corresponds to the inlet molar flow of CO_2 and W (g) to the total mass of catalyst, assuming a CSTR model:

$$r\ (mol\ CO_2.s^{-1}.\ g^{-1}) = CO_2\ conversion \cdot F_{CO_2,inlet} \cdot (1/W) \qquad \text{(Equation 1)}$$

3. Results and discussion

3.1. Textural and structural properties of the calcined samples

The first columns of **Table 1** list the labels and Ni contents measured by XRF for the series of prepared materials. The Table also details their mean pores volumes (micropores and mesopores) and surface area deduced from N_2 sorption measurements carried out on calcined and reduced samples. The corresponding isotherms are shown in **Figure 1.**

Table 1. *Textural and surface properties of the prepared samples*

Materials		**Ni content[a] (wt.%)**	**Textural properties[b]**			**Surface properties**	
			V_{micro} ($cm^3.g^{-1}$)	**V_{meso} ($cm^3.g^{-1}$)**	**S_{BET} ($m^2.g^{-1}$)**	**h index[c]**	**Amount of adsorbed CO_2 ($cm^3.g^{-1}$)[d]**
Alumina-based	MIL-53	-	0.40	0.40	1130	-	-
	Ni_5-$Al_2O_{3\text{-MIL-53}}$	5.1	0.05 (<0.01)	0.97 (0.85)	223 (225)	0.64	
	Ni_{15}-$Al_2O_{3\text{-MIL-53}}$	14.7	<0.01	1.09 (0.96)	251 (250)	0.60	8.2 (17.1)
	Ni_{20}-$Al_2O_{3\text{-MIL-53}}$	19.5	<0.01	1.05 (0.71)	245 (175)	0.58	16 (28)
	Ni_{15}-$Al_2O_{3\text{-OP}}$	14.2	<0.01	0.13 (0.11)	60 (44)	0.38	5.5 (9.6)
	Ni_{25}/γ-Al_2O_3*	25	<0.01	0.45 (0.42)	229 (103)	0.77	15.4 (24.4)
Silica-based	Ni_{15}/USY	14.5	0.16 (<0.01)	0.20 (0.25)	259 (261)	0.87	14 (23.3)
	Ni_{15}/SBA-15	14.5	0.11 (<0.01)	0.66 (0.62)	487 (422)	0.98	9.7 (21.1)

a: Ni content in the calcined dehydrated materials as estimated by XRF
b: as estimated from N_2 adsorption measurements for the calcined and reduced (in brackets) samples
c: ratio of the water weight losses during TG analysis after heating at 150 °C and 400 °C, respectively
d: amount of CO_2 adsorbed at 0 °C at P/P_0 partial pressures of 0.01 and 0.3 (in brackets)
*: Commercial sample.

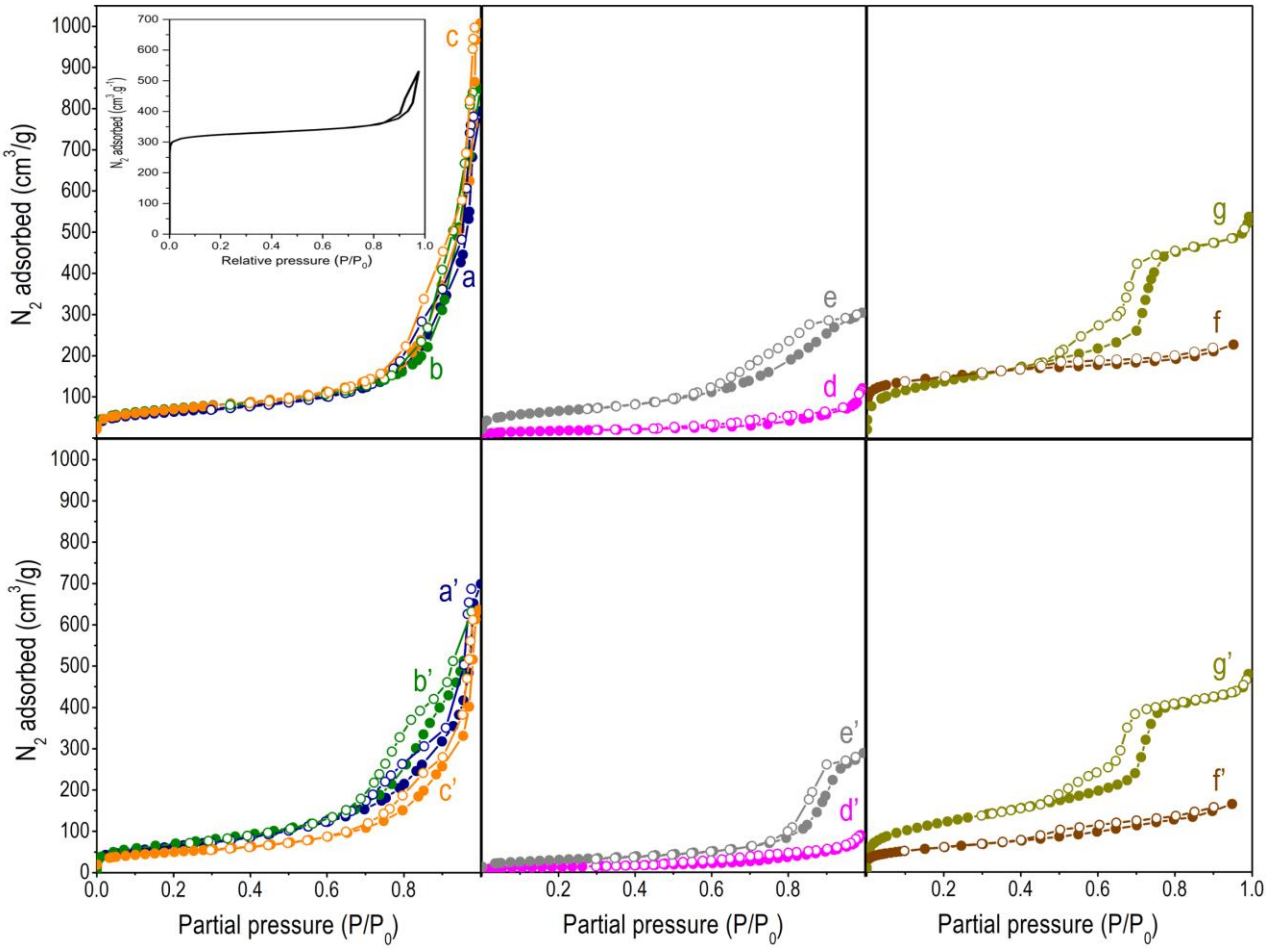

Figure 1: *N_2 physisorption isotherms of (a-g) calcined and (a'-g') reduced samples: (a,a') Ni_5-Al_2O_3-$_{MIL-53}$, (b,b') Ni_{15}-Al_2O_3-$_{MIL-53}$, (c,c') Ni_{20}-Al_2O_3-$_{MIL-53}$, (d,d') Ni_{15}-$Al_2O_{3\text{-}OP}$, (e,e') Ni_{25}/γ-Al_2O_3, (f,f') Ni_{15}/USY and (g,g') Ni_{15}/SBA-15. The inset shows the isotherm of the parent MIL-53 support.*

As commonly expected for a MOF material, the parent activated MIL-53 exhibits a type I isotherm characteristic of a microporous material and a very high surface area, above 1100 $m^2.g^{-1}$ (inset in **Fig. 1** and **Table 1**). Its impregnation with 5 wt% Ni followed by linkers decomposition results in the loss of the micropores and in a decrease of the specific area by a factor of about 5, as already discussed in more details in our recent paper [24]. Nevertheless, the total pore volume is simultaneously increased by 20% (**Table 1**) due to the formation of external meso/macro pores between the aggregated nanocrystals. This is attested by the type IV isotherms whose slit-type hysteresis loop in the 0.75 - 0.9 relative pressures range and marked step at relative pressures above $P/P_0 = 0.9$ are typical of a layered mesoporous material (**Fig. 1a**). Increasing the Ni amount from 5 wt.% to 15 wt.% (**Fig. 1b**) and then to 20 wt.% (**Fig. 1c**) does not alter the shape of the isotherm nor the surface area (220-250 $m^2.g^{-1}$) and total pores volumes (0.97-1.09 $cm^3.g^{-1}$) that are close in all calcined Ni_x-$Al_2O_{3\text{-}MIL53}$ materials (**Table 1**) and higher than in the comparative ordered mesoporous Ni_{15}-$Al_2O_{3\text{-}OP}$ sample obtained by one-pot-

EISA method (**Fig. 1d**). For the latter, it is worth noting that its porous properties (60 $m^2.g^{-1}$, 0.13 $cm^3.g^{-1}$) are significantly lower than those reported in our previous study for a one-pot-EISA synthesized sample prepared under the same conditions [19,25], but this is most probably due to the 3 times higher Ni content used here, that changed the Ni precursor concentration in the synthesis medium (change of pH), potentially affecting the structuring process during formation of the material. The total pore volumes are also systematically higher in the Ni_x-$Al_2O_{3\text{-}MIL53}$ samples compared to those in the silica-based references (Table 1), which are as expected either microporous (Ni_{15}/USY zeolite, type I isotherm, **Fig. 1f**) or mesoporous with a narrow distribution of large mesopores (Ni_{15}/SBA-15, type IV isotherm with a H1 type hysteresis loop at P/P_0 between 0.75 and 1, **Fig. 1g**).

The existence of an intergranular porosity in all the samples of the Ni_x-$Al_2O_{3\text{-}MIL\text{-}53}$ series is confirmed by transmission electron microscopy, as shown by the representative HR-TEM images of calcined Ni_5-$Al_2O_{3\text{-}MIL\text{-}53}$ (**Fig. 2A**) and Ni_{15}-$Al_2O_{3\text{-}MIL\text{-}53}$ (**Fig. 2B**). Whatever the Ni content, the sample appears as randomly interwoven nanosheets with ill-defined shapes and size of approximately 20-50 nm in length (see insets in **Fig. 2A** and **2B**). Although Ni is known to be present (because being introduced by incipient wetness impregnation), the images do not permit to detect any nickel-based particles (expected to appear darker than the support, if they exist), which suggests an excellent metal dispersion even at high metal loading (Ni_{15}-$Al_2O_{3\text{-}MIL\text{-}53}$).

A first evidence of the presence of nickel in the MOF-derived materials is however given by electron diffraction (SAED), as illustrated considering a selected area of a HR-TEM image of Ni_5-$Al_2O_{3\text{-}MIL\text{-}53}$ (**Fig. 2A'**). Its associated SAED picture (**Fig.2A"**) exhibits two distinct rings at distances d1 =1.8 Å (first ring) and d2= 1.3 Å (second ring) characteristic of reticular distances present in the spinel $NiAl_2O_4$ structure which consists of an ensemble of tetrahedral sites occupied by bivalent Ni^{2+} and of octahedral sites occupied by trivalent Al^{3+} cations [34,35].

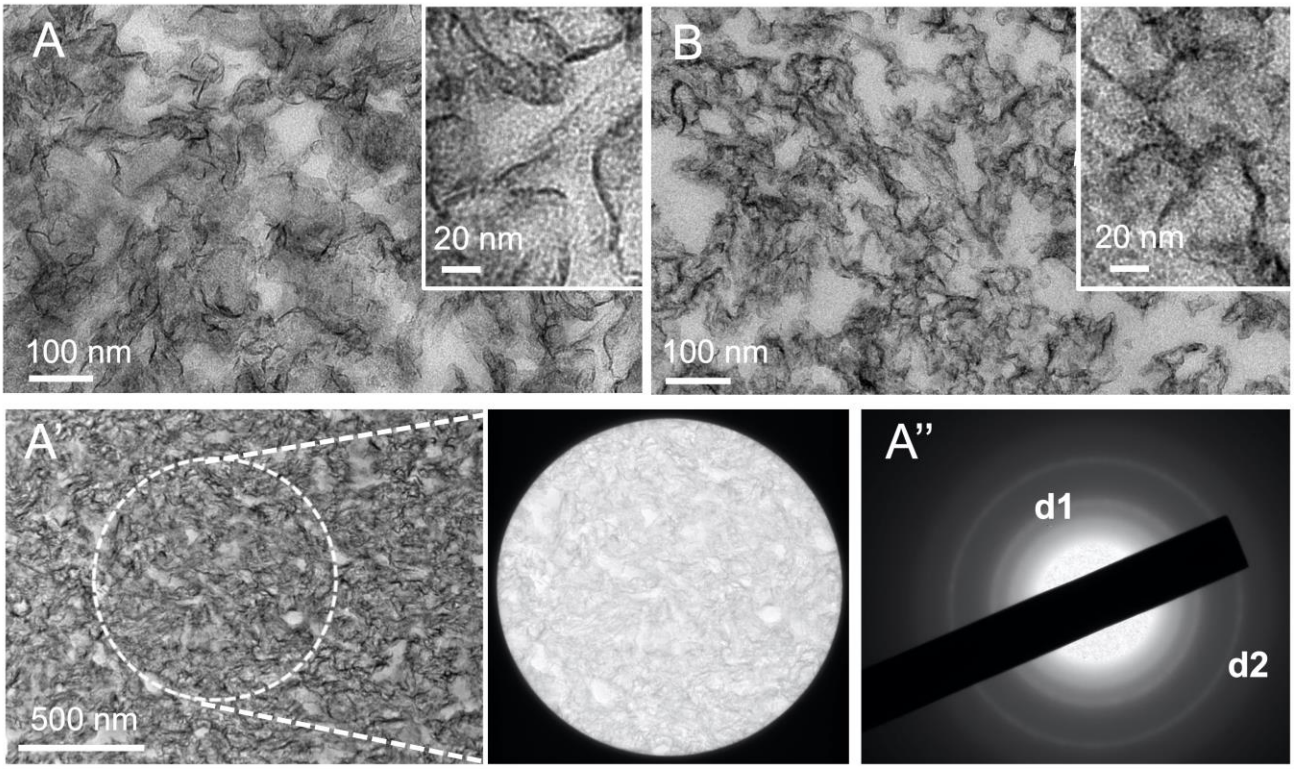

Figure 2. *HR-TEM micrographs of calcined (A,A') Ni_5-$Al_2O_{3\text{-}MIL\text{-}53}$ and (B) Ni_{15}-$Al_2O_{3\text{-}MIL\text{-}53}$ and (A'') local SAED image for a selected low magnification zone of calcined Ni_5-$Al_2O_{3\text{-}MIL\text{-}53}$; arrows indicate interwoven nanosheets layers.*

The occurrence of such Ni-rich spinel phase in all the calcined Ni_x-$Al_2O_{3\text{-}MIL\text{-}53}$ samples is also revealed by XRD patterns. For Ni_5-$Al_2O_{3\text{-}MIL\text{-}53}$ (**Fig. 3a**), three broad and tiny peaks at 2θ around 37.0°, 45.0° and 65.6° are indeed visible, assignable to the (220), (400) and (440) planes of cubic spinel $NiAl_2O_4$ (JCPDS: 001-1299). Such phase formation reveals an intimate mixing between Ni and its alumina-based support, demonstrating that the impregnation of nickel nitrate in the parent MIL-53 with high surface area enabled an efficient dispersion of the nickel precursor along the $[Al(OH)O_4]_n$ chains decorating the pores of MIL-53(Al). The close proximity between the Ni^{2+} and the preformed octahedral Al^{3+} sites of the MIL-53(Al) inorganic chains after impregnation is indeed believed to promote the formation of the spinel $NiAl_2O_4$ phase after the MOF calcination step (organic removal) [24,25]. Note also that the $NiAl_2O_4$ zones represent only a part of the material (because of limited Ni loading) and must be existing as crystalline nanodomains homogeneously dispersed within an amorphous alumina matrix (no XRD signal).

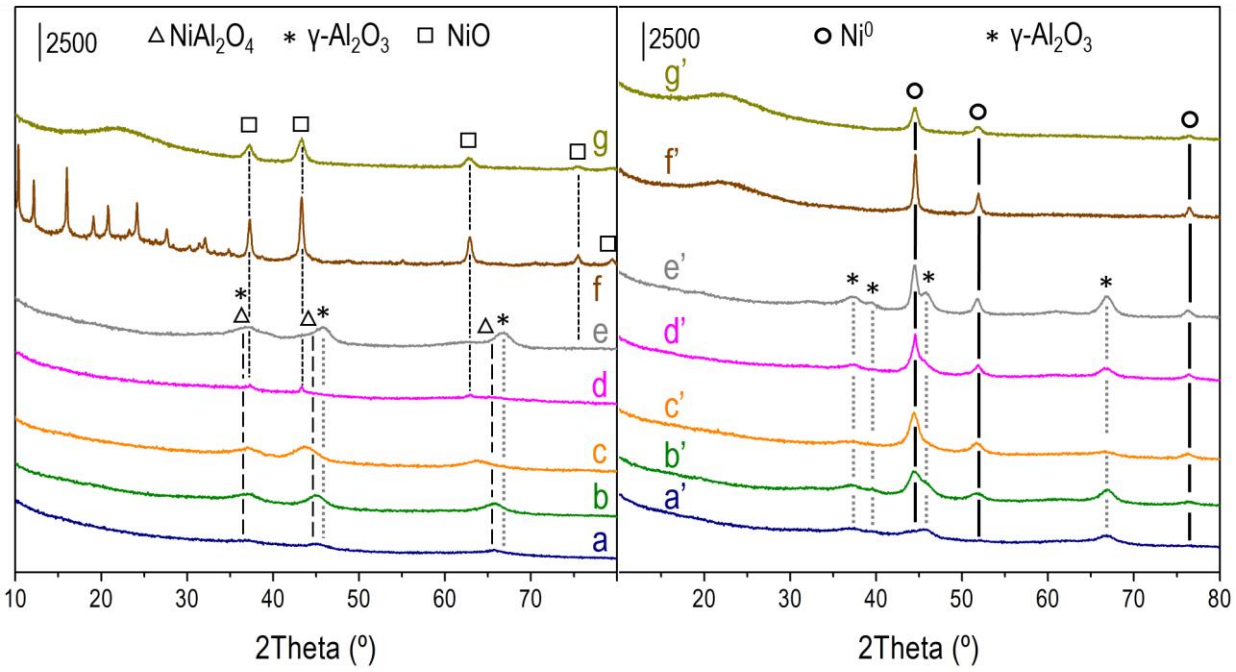

Figure 3. *XRD patterns of (a-g) calcined and (a'-g') reduced samples: (a-a') Ni_5-$Al_2O_{3\text{-}MIL\text{-}53}$, (b-b') Ni_{15}-$Al_2O_{3\text{-}MIL\text{-}53}$, (c-c') Ni_{20}-$Al_2O_{3\text{-}MIL\text{-}53}$, (d-d') Ni_{15}-$Al_2O_{3\text{-}OP}$, (e-e') Ni_{25}/γ-Al_2O_3, (f,f') Ni_{15}/USY and (g,g') Ni_{15}/SBA-15.*

For Ni_{15}-$Al_2O_{3\text{-}MIL53}$ (**Fig. 3b**), the diffraction peaks are still positioned at the same angles but they are more intense and thinner, revealing a higher number of bigger $NiAl_2O_4$ crystalline domains. Their mean size estimated by Scherrer's equation from the most intense peak (2θ=45°) is approximately 3 nm (**Table 2**). Upon further increase of the Ni content (Ni_{20}-$Al_2O_{3\text{-}MIL53}$, **Fig. 3c**), the three peaks start to shift to lower 2θ values, at positions equal to 37°, 44° and 62.8° that approach those of the (111), (200) and (220) planes of cubic NiO (JCPDS: 01-071-4750). This suggests that Ni is still highly dispersed and bonded to alumina, but crystalline NiO nanoparticles and spinel $NiAl_2O_4$ nanodomains coexist. Such coexistence is also detected in mesoporous Ni_{15}-$Al_2O_{3\text{-}OP}$ (**Fig. 3d**). For the latter, it is worth noting that only $NiAl_2O_4$ was detected in the mesoporous one-pot-EISA synthetized Ni-alumina sample with 5 wt% Ni prepared in our previous work [19,24,25], revealing some Ni extraction from the walls when more Ni is present. This can also be a consequence of the loss of structural ordering deduced above from N_2 physisorption data. With regard to the commercial catalyst Ni_{25}/γ-Al_2O_3, its diffractogram is typical of gamma alumina. The broadness of the peaks nevertheless suggests the possible existence of $NiAl_2O_4$. Also, a bump at 2θ of approximately 63° also indicates the presence in the sample of a small amount of NiO (**Fig. 3e**). Turning to the reference silica-based samples, the patterns reveal the presence of crystalline Ni-based nanoparticles in the form of only NiO (**Fig. 3f, g**) and the peaks are thin and intense, indicating a much lower Ni dispersion than in the above alumina-based materials (**Table 2**). This is especially the case of Ni_{15}/USY (**Fig. 3f**) which XRD pattern shows, in addition, thin peaks characteristic of the zeolite support for 2θ values below 35°(IZA database).

Table 2. *Properties of the nickel-based species: mean sizes of the crystalline domains, reducibility and number of surface sites.*

Materials	Mean size of the Ni-based nanocrystals (nm)		Reducibility of calcined materials[c]		Ni surface sites[d] ($mol_{Ni\ exposed}/g_{catalyst}$)	TOF[e] (s^{-1})
	Calcined[a]	Reduced[b]	T_{max} (°C)	H_2 uptake ($\mu mol.g^{-1}$)		
Ni_5-$Al_2O_{3\text{-}MIL53}$	-	- (7)	750	918	$2.4.10^{-5}$	0.252
Ni_{15}-$Al_2O_{3\text{-}MIL53}$	3*	6 (8)	720	2148	$6.0.10^{-5}$	0.320
Ni_{20}-$Al_2O_{3\text{-}MIL53}$	4*	7 (9)	700	3263	$7.3.10^{-5}$	0.335
Ni_{15}-$Al_2O_{3\text{-}OP}$	9*	9 (9)	375/650	1946	$5.3.10^{-5}$	0.049
Ni_{25}/γ-Al_2O_3	-	11 (12)	350/500/750	4174	$5.8.10^{-5}$	0.197
Ni_{15}/USY	17	19 (22)	375/600	2042	$1.9.10^{-5}$	0.279
Ni_{15}/SBA-15	8 (11)	10 (14)	375/600	2555	$2.9.10^{-5}$	0.103

a: mean size of the NiO and/or Ni_2AlO_4 (*) nanocrystals in the calcined samples as evaluated by XRD (see the experimental section for details)
b: mean size of the Ni^0 nanoparticles in the reduced catalysts as estimated by XRD or TEM (in brackets)
c: temperature of peaks maxima and total H_2 consumption during TPR experiments; the theoretical H_2-uptake is 860 $\mu mol.g^{-1}$ for a sample with 5 wt% Ni.
d: g_{cat} × Ni loading × dispersion/Ni atomic weight
e: TOF values calculated at a temperature of 300 °C.

3.2. Surface properties

It is well known that H_2O can have an inhibitory effect during CO_2 methanation [8]. On one hand, water is a reaction product that can displace the equilibrium towards the formation of carbon dioxide, due to the reversibility of the Sabatier reaction, which inhibits CO_2 conversion. On another hand, water can compete with CO_2 for adsorption on the same sites [27,36,37], thus characterizing the affinity of the catalysts with water is therefore of interest. To this end, TGA experiments were carried out (**Fig.S1**) on the catalysts after their saturation with water to determine the hydrophobicity (h) index. This parameter, calculated as the ratio of the amount of weakly adsorbed water molecules over that of all adsorbed water molecules (desorbed at 150°C and 400°C temperature, respectively), gives an information about the strength of interaction between water and the surface (the higher the h index, the higher the surface hydrophobicity) [30]. The h index values determined for the different Ni_x-$Al_2O_{3\text{-}MIL\text{-}53}$ samples (**Table 1**) are similar (~0.6 in all cases) and tend to slightly decrease with the increase of the Ni content. In view of this value, which is significantly below 1, the interaction of the produced water with the surface of the MOF-derived Ni-alumina materials is not negligible but it is comparable among the three samples, independent of Ni loading. The strength of water adsorption is even more important on mesoporous Ni_{15}-$Al_2O_{3\text{-}OP}$ (h index = 0.38), which suggests a higher proportion of surface OH defect sites at the surface of the walls of the mesoporous hexagonal structure, probably leading to a higher inhibitory effect of the formed water during reaction. By comparison, the commercial and silica-based samples are all more hydrophobic, and their h indexes vary from 0.77 (Ni_{25}/γ-Al_2O_3) to

0.87 (Ni_{15}/USY) and 0.98 (Ni_{15}/SBA-15), in line (last two samples) with what is expected for silica-based ordered materials.

Another surface property that can impact the performances of the catalysts is their capacity to adsorb CO_2 since carbon dioxide adsorption is a key step in the CO_2 methanation reaction [38,39]. This affinity was compared based on the chemical nature of the support by collecting CO_2 adsorption isotherms (at 0°C) on the four calcined samples with same 15 wt% Ni content (**Fig. 4)**. The CO_2 uptakes at P/P_0=0.3 follow the order of: Ni_{15}/USY > Ni_{15}/SBA-15 > Ni_{15}-$Al_2O_{3\text{-MIL-53}}$ > 15Ni-$Al_2O_{3\text{-OP}}$. The higher uptakes for both silica-based materials (**Fig. 4c,d**) can be explained by their higher amount of micropores (especially in Ni_{15}/USY) and higher specific surfaces (especially in Ni_{15}/SBA-15) compared to the alumina-based samples (**Table 1**), both aspects being favourable to CO_2 adsorption. For the Ni_{15}/USY zeolite sample, an additional positive feature could be the presence of framework compensating cations, even if in low amount (Si/Al ratio equal to 38), that can strongly interact with carbon dioxide [27]**.** By comparison, none of the alumina materials contain micropores and their specific surface, although important, is mainly associated to an intergranular mesoporosity. However, at lower pressure, the tendency to adsorb CO_2 is the highest for the MOF-derived Ni_{15}-$Al_2O_{3\text{-MIL-53}}$ sample (**Fig. 4a, right**) and next for Ni_{15}-$Al_2O_{3\text{-OP}}$ material. This faster CO_2 adsorption, indicative of the existence of some stronger adsorption sites on the alumina supports, might play a role during catalysis that involves a dynamic adsorption/activation process.

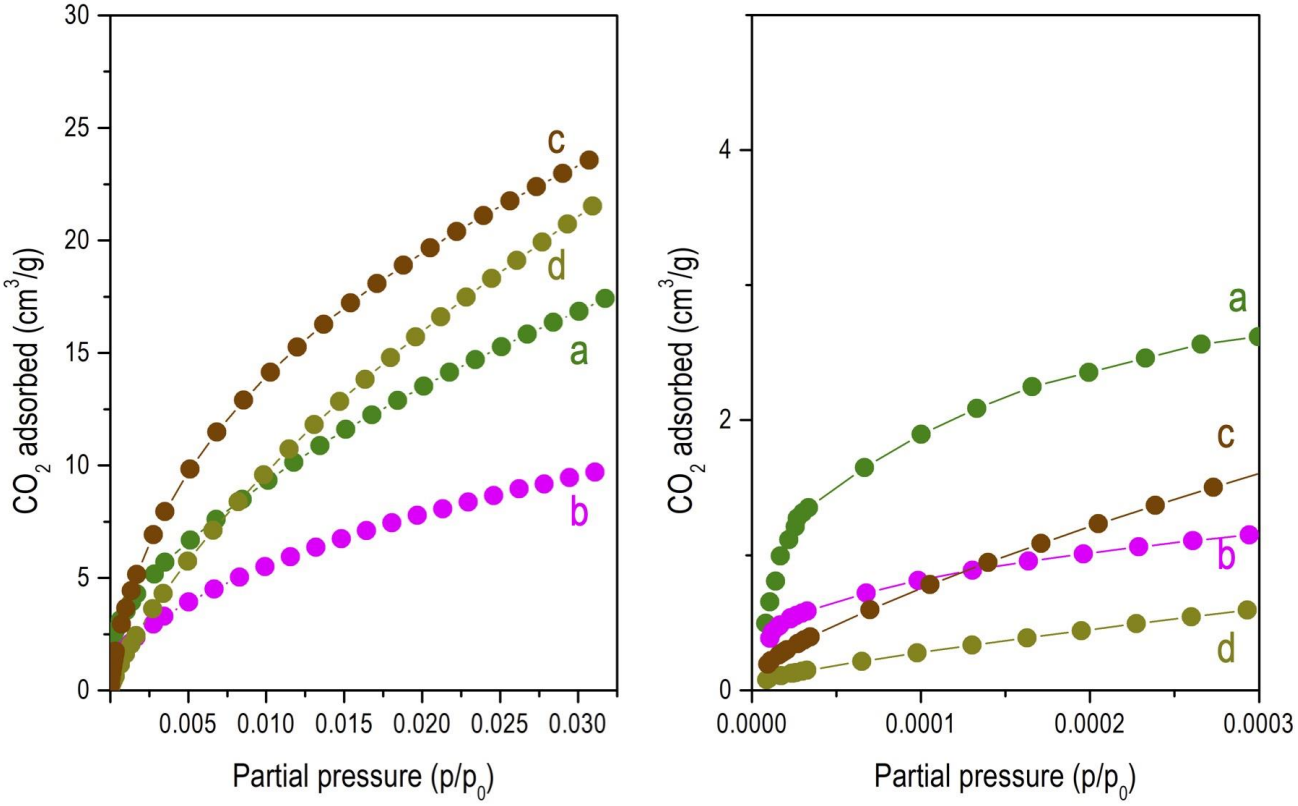

***Figure 4**. CO_2 adsorption isotherms collected on calcined (a) Ni_{15}-$Al_2O_{3\text{-}MIL\text{-}53}$, (b) Ni_{15}-$Al_2O_{3\text{-}OP}$, (c) Ni_{15}/USY, (d) Ni_{15}/SBA-15; P/P_0 between 0 to 0.03 (left) and zoom between 0 and 0.0003 (right)*

3.3. Reducibility of the nickel-based species

The reducibility of the calcined materials was investigated by H_2-TPR measurements. During this treatment, the oxidized nickel species present in the materials are expected to be transformed to metallic Ni^0, the nickel state responsible for H_2 dissociation in the CO_2 methanation reaction. For all Ni_x-$Al_2O_{3\text{-}MIL\text{-}53}$ samples, the reduction profiles are very similar (**Fig. 5Aa-c**), with only one peak at high temperature (650-800 ºC), typical of Ni ions strongly interacting with the alumina phase such as Ni^{2+} in $NiAl_2O_4$ [24,40]. Notably, no peak is detected at temperatures below 500°C, which attests of the absence of NiO nanoparticles weakly attached on the alumina support [40]. A progressive small displacement of the peak towards lower temperatures is nevertheless observed when increasing the Ni loading, revealing a tendency of the Ni-based species to be more and more reducible as the sample becomes Ni-richer. All these features are in good agreement with the above HR-TEM and XRD data that revealed a high nickel dispersion in the form of mainly $NiAl_2O_4$ in Ni_5-$Al_2O_{3\text{-}MIL\text{-}53}$ but a coexistence of $NiAl_2O_4$ and (more reducible) NiO-like species as the Ni loading is raised (Ni_{20}-$Al_2O_{3\text{-}MIL\text{-}53}$) (**Fig. 3c**). The still high reduction temperature for the latter sample (T = 690°C) shows that the NiO species strongly interacts with the surface of the alumina walls and does not consist of free NiO particles weakly attached to the support. The occurrence of only one peak for this sample, moreover, suggests that the NiO and $NiAl_2O_4$ nanoparticles are not distinct but rather consist of a defective Ni aluminate phase whose flexible structure is related to both NiO and $NiAl_2O_4$.

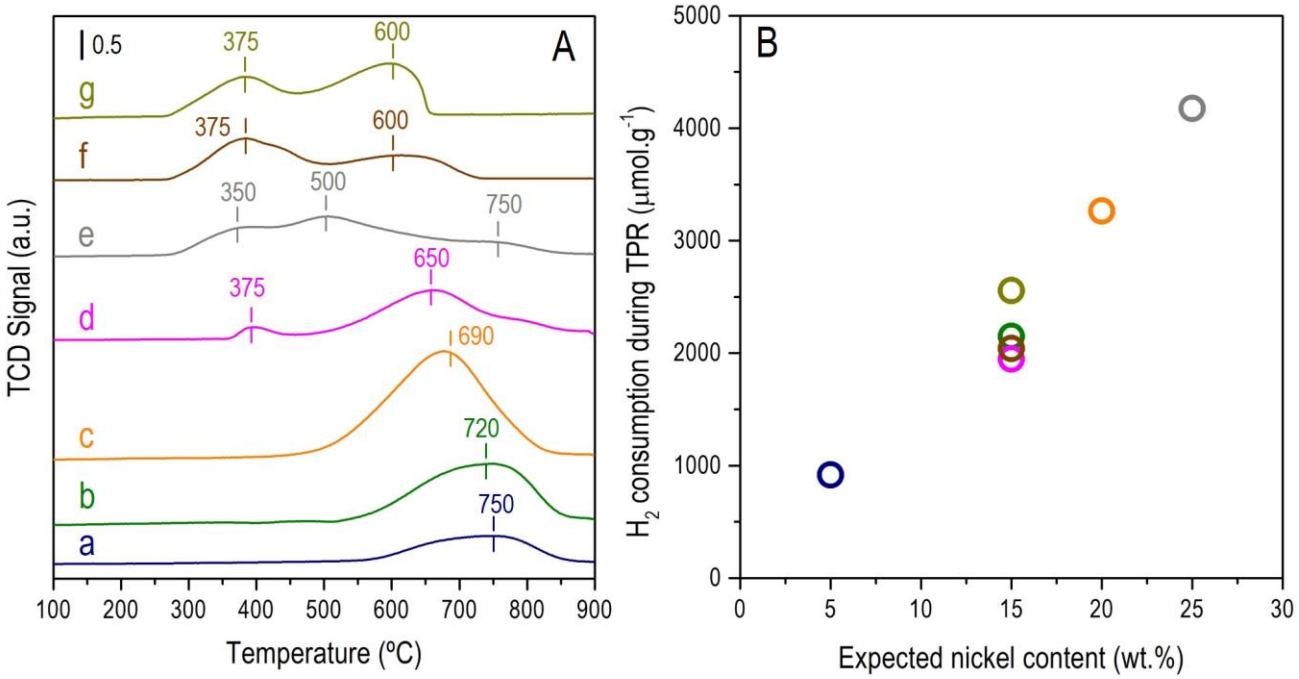

Figure 5. *(A) H_2-TPR profiles of calcined samples: (a) Ni_5-$Al_2O_{3\text{-}MIL\text{-}53}$, (b) Ni_{15}-$Al_2O_{3\text{-}MIL\text{-}53}$, (c) Ni_{20}-$Al_2O_{3\text{-}MIL\text{-}53}$, (d) Ni_{15}-$Al_2O_{3\text{-}OP}$, (e) Ni_{25}/γ-Al_2O_3, (f) Ni_{15}/USY and (g) Ni_{15}/SBA-15. (B) Experimental H_2 uptakes as a function of the impregnated Ni content: Ni_5-$Al_2O_{3\text{-}MIL\text{-}53}$ (dark blue), Ni_{15}-$Al_2O_{3\text{-}MIL\text{-}53}$ (dark green), Ni_{20}-$Al_2O_{3\text{-}MIL\text{-}53}$ (orange), Ni_{15}-$Al_2O_{3\text{-}OP}$ (rose), Ni_{15}/USY (brown), Ni_{15}/SBA-15 (army green) and Ni_{25}/γ-Al_2O_3 (grey).*

For Ni_{15}-$Al_2O_{3\text{-}OP}$ (**Fig. 5d**), a main peak at high temperature (~700 ºC) is still observed, but it is accompanied by a less intense one centred at ~400 ºC typical of the reduction of NiO species weakly interacting with the Al_2O_3 matrix, which fully agrees with the above XRD detection of crystalline NiO in this sample. For commercial Ni_{25}/γ-Al_2O_3 (**Fig. 5e**), reduction at lower temperature prevails, suggesting that the NiO species are weakly bounded, probably due to the combination of a slightly higher Ni content and intermediate pore volume (**Table 1**) that drive Ni to sinter in this sample. For both Si-based Ni_{15}/USY and Ni_{15}/SBA-15 (**Fig. 5f, g**), two peaks are also systematically seen, at low (T< 500 °C) and high (T> 500 °C) temperature range, assignable to NiO nanoparticles located on the surface of the silica (zeolite of SBA-15) grains and trapped in the pores, respectively. In the case of Ni_{15}/USY, the high temperature peak may also involve the reduction of Ni^{2+} cations positioned at framework compensating sites in the zeolite sample [41,42].

It is also important to note that, for all materials, the amount of H_2 consumed between 200 and 900 °C during the TPR experiment (values reported in **Table 2**) is in very good agreement with the theoretical H_2-uptake expected when considering the Ni loading and assuming a bivalent Ni oxidation state in the calcined samples. This agreement is better shown by the linear correlation obtained when reporting these H_2-upatkes as a function of the amount of impregnated nickel (**Fig. 5B**).

3.4. Dispersion and distribution of the Ni^0 nanoparticles

The evolution of the state of the Ni-based species after reduction was analysed from the X-Ray diffractograms of the reduced materials reported in **Figure 3** together with those before reduction (already discussed above). For all MOF-based materials (**Fig. 3a'-c'**), the reduction treatment contributed to the formation of new diffraction peaks at 2θ of 44.5°, 51.9° and 76° attributed to the (111), (200) and (220) planes of crystalline Ni^0, respectively (JCPDS: 03-065-0380). In addition, bands typical of γ-Al_2O_3 systematically appear, asserting on the segregation of the crystalline $NiAl_2O_4$ nanospecies into metallic Ni^0 and alumina. The isolated peak at 51.9° was used to evaluate the mean Ni^0 nanoparticle sizes (by Scherrer's equation), leading to values between 6 and 7 nm (**Table 2**).

These mean sizes values are also in good agreement, even if slightly smaller, with those estimated from the histograms of particle sizes established by measuring the size of approximately 500 nanoparticles in HR-TEM images, (**Fig. 6**, **Table 2**). Despite the good resolution of the HR-TEM images, this discrepancy could be due to contrast issues making the detection of the smallest nanoparticles (2-4 nm) on the alumina grains uneasy by this technique. The histograms of Ni^0 particles sizes visualize well the Ni^0 particles sizes distribution and its tendency to shift towards higher sizes when more nickel is present in the Ni^0_x-$Al_2O_{3\text{-MIL53}}$ catalysts (**Fig. 6a'-c'**). Nevertheless, the mean size of 9.4 nm in Ni^0_{20}-$Al_2O_{3\text{-MIL53}}$ with the highest Ni loading remains significantly below the value of 12 nm evaluated for the commercial Ni_{25}/γ-Al_2O_3 catalyst (**Fig. 6d'**).

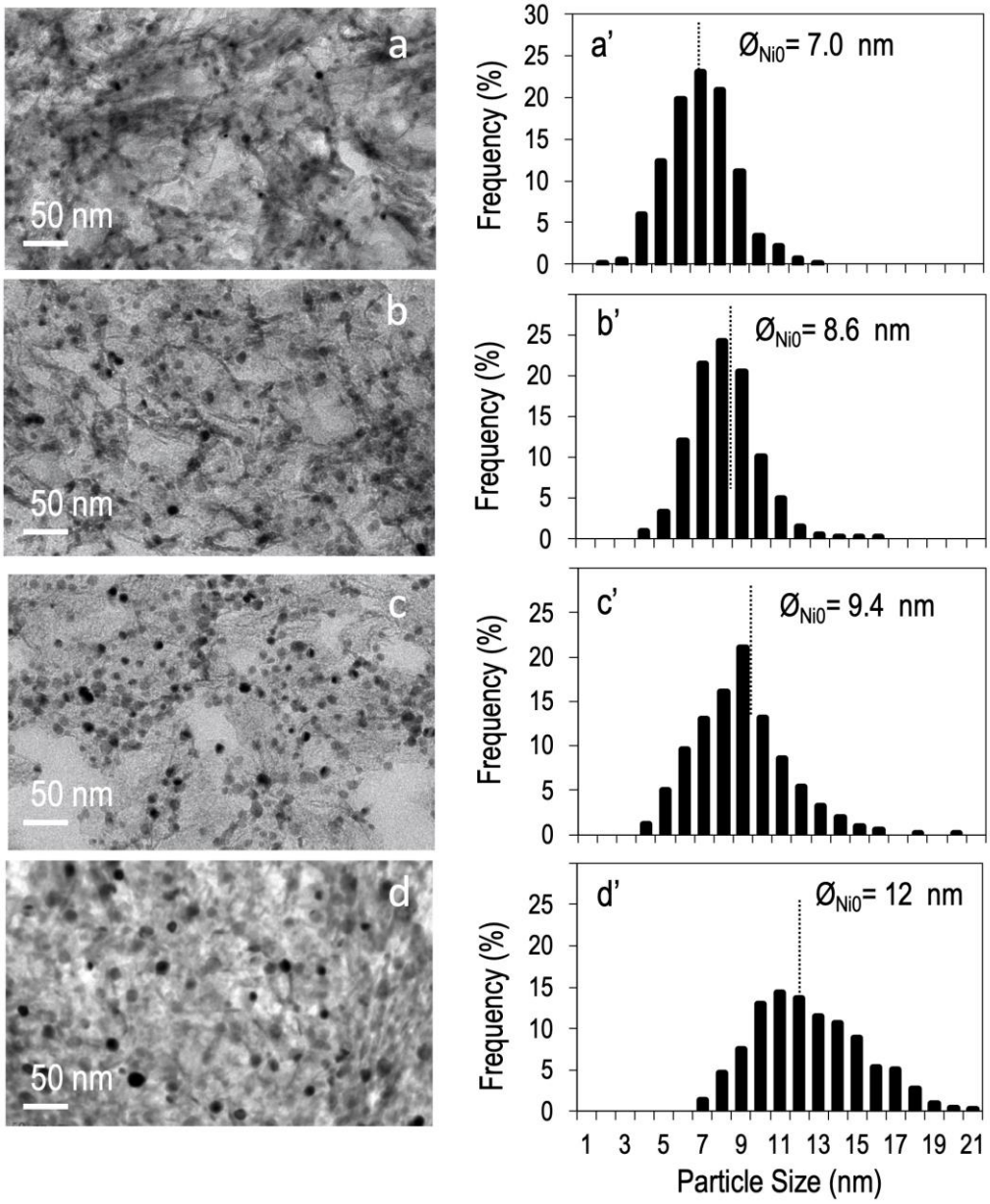

Figure 6*. (a-d) HR-TEM micrographs and (a'-d') distribution of particles sizes in reduced (a,a') Ni_5-$Al_2O_{3\text{-}MIL\text{-}53}$, (b,b') Ni_{15}-$Al_2O_{3\text{-}MIL\text{-}53}$, (c,c') Ni_{20}-$Al_2O_{3\text{-}MIL\text{-}53}$ and (d,d') Ni_{25}/γ-Al_2O_3.*

These values are moreover smaller than the sizes of Ni^0 in both silica-based catalysts in which mean sizes of 14 nm (Ni_{15}/SBA-15) and even 22 nm (Ni_{15}/USY) are reached as seen in the micrographs (**Fig. S2** in supplementary information) and X-Ray diffractograms of the samples (thinner peaks of Ni^0 in **Fig. 3f',g'**). Such lower nickel dispersion on the silica supports, especially on the zeolitic one, agrees with the weaker metal-support interaction depicted from H_2-TPR and already tackled in literature when comparing oxides others than alumina, like ZrO_2, TiO_2 or SiO_2, as nickel supports [43]. It is also worth noting that the sizes in the Ni^0_x-$Al_2O_{3\text{-}MIL53}$ series of catalysts are below than those previously reported in the literature for metallic nanoparticles supported on other MOF-based materials (between 9 and 20 nm) [23,44]. All these features show that the strategy of occluding nickel inside the pores of MIL-53

before calcining it to form the alumina support is an efficient route to produce small nickel particles, even at high nickel loadings highlighting the benefit of using MIL-53(Al) both as nickel support and alumina precursor for the preparation of a nickel alumina catalyst with improved nickel dispersion.

Moreover, in the three Ni^0_x-$Al_2O_{3\text{-}MIL53}$ catalysts, and independently of the nickel loading, the metal nanoparticles always appear homogeneously dispersed over the alumina support that still takes the form of interwoven nanosheets (**Fig. 3a-c**). Such preservation of the textural properties after reduction is also deduced from the N_2 sorption isotherms of the Ni^0_x-$Al_2O_{3\text{-}MIL53}$ catalysts that still exhibit a type IV-related physisorption profile with a slit-like hysteresis typical of a layered material with unorganized interlayered pores (**Fig. 1a'-c'**). The specific surfaces deduced from the curves are however slightly decreased compared to those in the calcined materials (**Table 1**), indicating that some – although limited – structural shrinkage occurred at the high reduction temperature of 800 °C. This is accompanied by a small increase of the diameters of pores, possibly attributable to the phase transformation of $NiAl_2O_4$ into γ-Al_2O_3 and to Ni^0 nanoparticles formation spacing apart the nanosheets one from another.

3.5. Catalytic performances

Figure 7 shows the results of catalytic measurements carried out in the same conditions (detailed in section 2.3) on all the catalysts. They are reported in terms of CO_2 conversion (**Fig. 7a-g**) and CH_4 selectivity (**Fig. 7a'-g'**) as a function of the reaction temperature (light-off curves). For all catalysts, the CO_2 conversion progressively increases with the temperature between c.a. 250 to 350°C, afterwards it starts decreasing because of attaining the thermodynamic equilibrium (dotted lines in **Fig. 7**) that is unfavourable to the reaction upon heating.

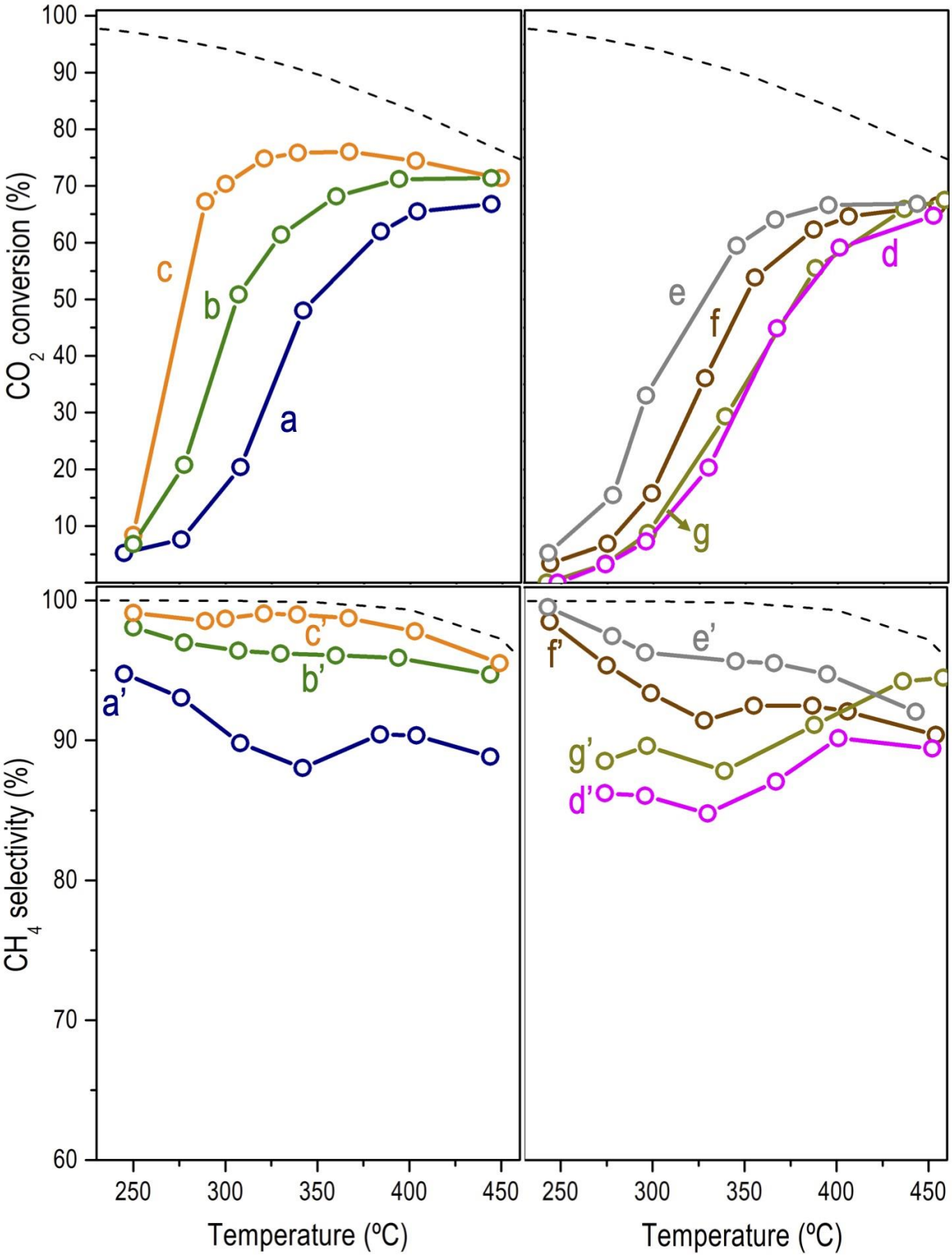

Figure 7. *(a-g) CO_2 conversions and (a'-g') CH_4 selectivity obtained at increasing temperatures during catalytic tests on reduced: (a,a') Ni_5-$Al_2O_{3\text{-}MIL\text{-}53}$, (b,b') Ni_{15}-$Al_2O_{3\text{-}MIL\text{-}53}$, (c,c') Ni_{20}-$Al_2O_{3\text{-}MIL\text{-}53}$, (d,d') Ni_{15}-$Al_2O_{3\text{-}OP}$, (e,e') Ni_{25}-γ-Al_2O_3, (f,f') Ni_{15}/USY and (g,g') Ni_{15}/SBA-15. The dotted black line corresponds to values at thermodynamic equilibrium.*

Before discussing in detail the catalytic performances revealed by the samples from the present work, some insights on CO_2 methanation (Sabatier) reaction mechanism over Ni/alumina catalysts must be mentioned. For instance, Cárdenas-Arenas et al. [45] verified by carrying out an isotopic and *in situ* DRIFTS study that the reaction starts through CO_2 chemisorption over hydroxyl groups created by H_2 reduction in the $NiO\text{-}Al_2O_3$ interface. Afterwards, the formation of H_2O and CO or CH_4 (both arising from formate species acting as intermediates) was verified. Authors concluded that CO_2 chemisorption/dissociation and H_2O formation occur on the same active sites. Consequently, the slower release of water as well as the accumulation of formate species in these sites limit the chemisorption and dissociation of further CO_2 molecules. Furthermore, Lim et al. [46] carried out a kinetic study using a batch reactor and considered a mechanism again initiated by CO_2 chemisorption and dissociation on the surface of the catalyst, leading to CO and O species. In this case, authors considered the dissociation of the adsorbed CO as the rate-limiting step. Finally, Vogt et al. [47] performed a theoretical study over Ni catalysts with Ni^0 particle sizes varying from 1 to 6 nm and again proposed the dissociation and further hydrogenation of CO as rate-limiting step.

When analysing the evolution of the CO_2 conversion in the $Ni_x\text{-}Al_2O_{3\text{-MIL-53}}$ series of catalysts (**Fig. 7a-c**), it is noticeable that CO_2 conversion increases linearly with respect to the nickel content. This trend is clearly visualized when plotting the CO_2 conversions obtained at 300°C as a function of the Ni weight percentages (pink hexagons**, Fig. 8**). To explain this linear relationship, it can be recalled

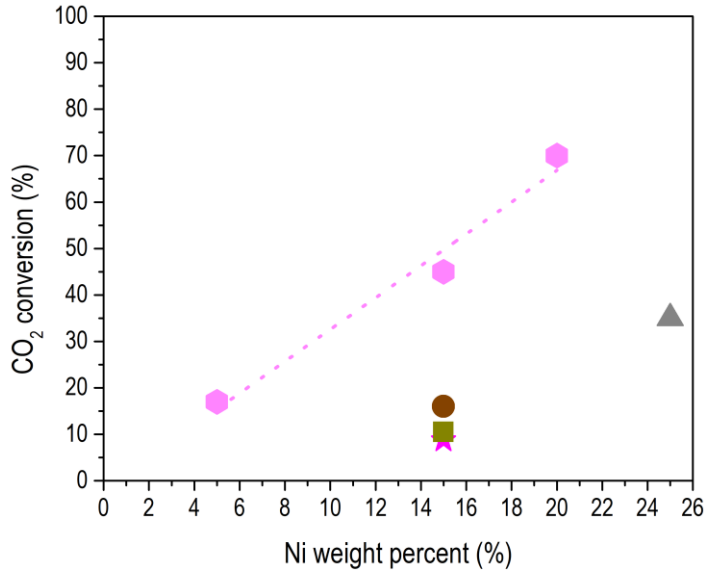

Figure 8. *CO_2 conversions at 300°C (at steady state conditions) as a function of the Ni weight percent in the prepared catalysts:* $Ni_x\text{-}Al_2O_{3\text{-MIL-53}}$ *(hexagons),* $Ni_{15}\text{-}Al_2O_{3\text{-OP}}$ *(star),* $Ni_2/\gamma\text{-}Al_2O_3$*, (triangle),* Ni_{15}/USY *(circle),* Ni_{15}/SBA-15 *(square)*

that (i) the nickel dispersion is comparable in all three catalysts, hence the number of Ni^0 surface atoms should be proportional to the Ni content, (ii) they exhibit close specific surfaces (alumina) for CO_2

adsorption and (iii) they are characterized by comparable h indexes which suggests a similar sensitivity to the inhibitory effect of water formed during reaction (**Table 1**). Consequently, it is expected that an increase in the number of available nickel sites for H_2 dissociation boosts the supply of H atoms, required for the hydrogenation of the CO_2 chemisorbed over the catalyst's surface.

The CO_2 conversion curves for the other catalysts (**Fig. 7d-g**) and their levels of conversions at 300°C (**Fig. 8**) clearly show that they are significantly less active than the MOF-derived Ni_x-$Al_2O_{3\text{-MIL-53}}$ catalysts. Amongst them, commercial Ni_{25}/γ-Al_2O_3 with the highest Ni content, reaches a level of CO_2 conversion at 300°C (triangle in **Fig. 8**) slightly below the one attained on Ni-poorer Ni_{15}-$Al_2O_{3\text{-MIL-53}}$. This lower catalytic activity might be explained by the lower Ni dispersion (by more than 25%) in Ni_{25}/γ-Al_2O_3 (**Table 2** and **Fig. 6**). The same reason could also contribute to the poor activities observed for both Ni_{15}/USY (**Fig. 7f**) and Ni_{15}/SBA-15 (**Fig. 7g**) but an additional effect might exist, on these two silica-based catalysts. Indeed, even if their hydrophobic character (high h index, **Table 2**) should be favourable (less inhibitory role of water) and if their capacity of adsorption of CO_2 at a P/P_0 pressure of 0.03 is higher than in the alumina sample (due to their higher pores volumes), the CO_2 adsorption is less favourable at very low pressure (**Fig. 4**), suggesting a more difficult CO_2 activation process on the silica supports. This would be in line with literature reporting that the SBA-15 support is not able to significantly adsorb and activate CO_2, and that both CO_2 adsorption/activation and H_2 dissociation are assumed to occur over the same Ni^0 active sites [48]. For the zeolitic catalysts, the CO_2 adsorption as carbonates could occur over the compensating cations [27,32] and on extra-framework aluminium species (EFAL) [39], which may explain the slightly better performances of this catalyst compared to Ni_{15}/SBA-15 (**Fig. 7f and 7g**). Turning now to the Ni_{15}-$Al_2O_{3\text{-OP}}$ catalyst, its very poor activity (**Fig. 7d** and star in **Fig. 8**) cannot be attributed to its metal dispersion (as good as in Ni_x-$Al_2O_{3\text{-MIL-53}}$) but rather to its poor textural properties (specific surface 4 times lower than in Ni_x-$Al_2O_{3\text{-MIL-53}}$) associated to a poor CO_2 adsorption capacity (**Fig. 4d**). The h index for this sample is also about two times lower (Table 2), revealing an enhanced inhibitory role of water. These results are quite consensus with the TOF values illustrated in Table 2. For MOF-derived Ni_x-$Al_2O_{3\text{-MIL-53}}$ catalysts, the increment of Ni loading did not affect TOF values and the TOF of Ni_{20}-$Al_2O_{3\text{-MIL-53}}$ (0.335 s^{-1}) containing 20 wt% Ni remains as good as the TOF of Ni_5-$Al_2O_{3\text{-MIL-53}}$ (0.252 s^{-1}) containing 5 wt% Ni. Not to mention that the latter samples possess higher TOF values than other catalysts having poorer metal dispersion and textural properties (Table 2).

To evaluate the performances of the catalysts, not only their activity but also their selectivity to the desired reaction (here CH_4) is important. Here, again, the MOF-derived Ni_x-$Al_2O_{3\text{-MIL-53}}$ catalysts are clearly the most performing, especially Ni_{15}-$Al_2O_{3\text{-MIL-53}}$ and Ni_{20}-$Al_2O_{3\text{-MIL-53}}$ that give always high

selectivity to CH_4, between 96 and 99%, whatever the temperature is (**Fig. 7b'-c'**). The selectivity is lower on the other catalysts, especially in the 300-350 ºC temperature range. Based on *Operando* FTIR studies reported in the literature for Ni-supported zeolites (aluminosilicates) [39], the reduction in CH_4 selectivity at 300-350 ºC could be explained by an accumulation of adsorbed CO/formate species (arising from CO_2 dissociation) over the catalysts surface, limiting its dissociation/hydrogenation.

For the sake of completion, the catalytic stability of the most performing Ni_{20}-$Al_2O_{3\text{-MIL-53}}$ catalyst was assessed by running the reaction for 10 or 20h at 350°C and comparing it to the stability of commercial Ni_{25}/γ-Al_2O_3 material tested in the same conditions (**Fig. 9**). This temperature was chosen, although given CO_2 conversion levels approaching those of thermodynamic equilibrium, to enhance eventual Ni deactivation processes by sintering, if existing. In agreement with the previous section, the performances were higher for both Ni_{15}-$Al_2O_{3\ \text{MIL-53}}$ and Ni_{20}-$Al_2O_{3\ \text{MIL-53}}$ (70-75% CO_2 conversion and 99 % CH_4 selectivity) than for Ni_{25}/γ-Al_2O_3 (60% CO_2 conversion and 95% CH_4 selectivity). More importantly, none of the catalysts suffered a noticeable deactivation during the test duration, neither in term of activity nor of selectivity. Moreover, the TEM micrograph collected for the spent Ni_{15}-$Al_2O_{3\ \text{MIL-53}}$ catalyst after undergoing the reaction for 20 h shows the conservation of both its textural properties and high nickel dispersion. The average Ni^0 particle size of 7.3 nm estimated from the histograms indicates an absence of metal sintering. This further proves that the Ni-Al_2O_3 catalysts derived from MIL-53 constitute interesting materials for CO_2 methanation reaction for the synthesis of CH_4 natural gas.

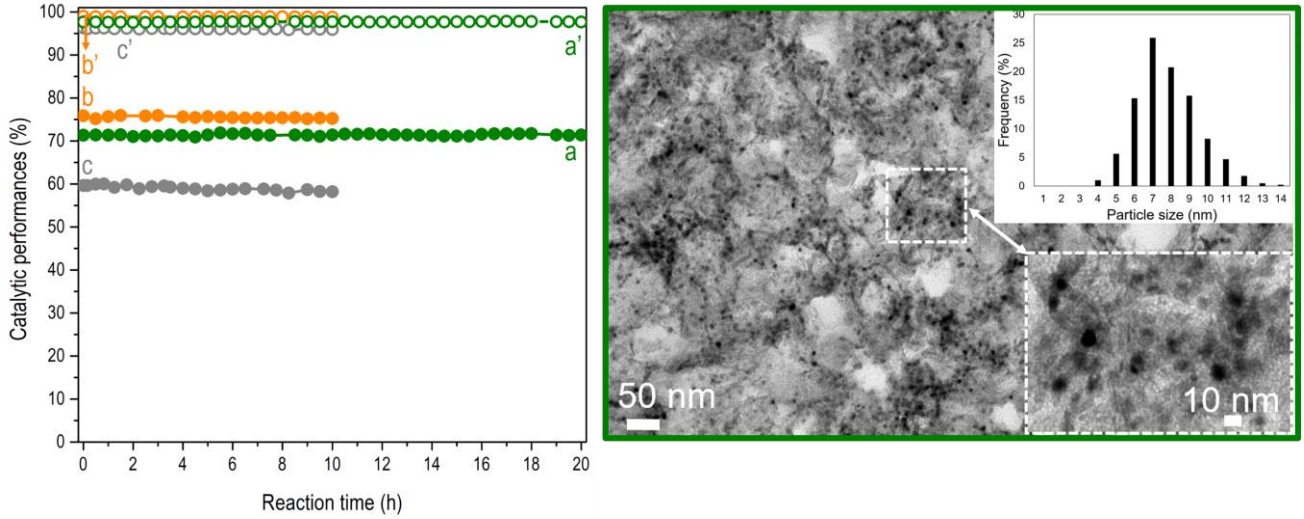

Figure 9. A. *Stability test results in terms of (a-c) CO_2 conversion and (a'-c') CH_4 selectivity of (a, a') Ni_{15}-$Al_2O_{3\text{-MIL-53}}$, (b, b') Ni_{20}-$Al_2O_{3\text{-MIL-53}}$ and (c,c') Ni_{25}/γ-Al_2O_3 over 10 or 20 h time on stream and B. TEM micrograph of spent Ni_{15}-$Al_2O_{3\text{-MIL-53}}$ after CO_2 methanation reaction. Conditions: T=350 °C, GHSV=1435 $ml.g^{-1}.min^{-1}$, H_2:CO_2= 4:1.*

Fig. 10 displays the obtained rates as a function of the reaction temperature of different Ni/support-based catalysts tested recently in literature in the CO_2 methanation reaction. As a final step, a comparison between the best MIL-53-derived catalyst and other Ni/support-based catalysts tested recently in literature towards CO_2 methanation reaction was intended. For this purpose, and taking into account that the conditions used in literature (e.g., mass of catalyst - W, inlet flow of CO_2 - $F_{CO2,inlet}$) were not the same, average CO_2 reaction rates (r) were determined far from the thermodynamic equilibrium and displayed in Fig. 10 as a function of the reaction temperature. From this comparison, our best performing catalyst that is Ni_{20}-$Al_2O_{3\text{-MIL-53}}$ is even better than Ni-Al_2O_3 materials prepared by "layered double hydroxide" or "EISA" method (**curves a,c, Fig.7**). Ni_{20}-$Al_2O_{3\text{-MIL-53}}$ possesses also better average CO_2 reaction rates than other Ni-supported materials reported in literature (**Fig. 7 curves b, c-l**) with a wide range of support types ranging from sepiolite, zeolite FDU, mesoporous silica MCM-41, fibrous nanosphere silica KCC carbon nanotubes CNT, zirconia ZrO_2, bentonite, metal oxide composites (CeO_2-ZrO_2, Al_2O_3-ZrO_2-TiO_2-CeO_2), and silicon carbide SiC. This highlights on the superior performance of the new catalyst prepared in this study over the existed ones in literature. Finally, the same trend is even observed when comparing the average CO_2 reaction rates calculated with Ni weight present in each catalyst (**Fig. S4**). The only difference concerns the sample supported on zirconia (**curve g, Fig. S4**) that displays better performances but which is however known to be more expensive than alumina.

The beneficial role of MIL-53 in the formation of catalysts with superior performances is mainly explained by the capacity of this hybrid framework to disperse the nickel precursors (nitrate salt) in close proximity to its Al(μ_2-OH) inorganic nodes [24]. This proximity of Ni^{2+} cations to octahedral coordinated trivalent Al^{3+} cations within the pores is assumed to favour the formation of nickel aluminate ($NiAl_2O_4$) nanodomains, a spinel phase which is also composed of an ensemble of tetrahedral coordination occupied with bivalent Ni^{2+} and octahedral coordinated Al^{3+} cations [34]. The thermal removal of the organic linkers then results in the formation of inorganic materials with high surface areas (Table 1), in which the $NiAl_2O_4$ nanodomains are highly dispersed and close to the surface. We believe that forming such well-dispersed $NiAl_2O_4$ nanodomains is a key step towards particularly active and stable catalysts for several reasons: (i) the occurrence of the Ni^{2+} cations isolated within the $NiAl_2O_3$ nanodomains is believed to slow down their extraction from the support during the reduction step, thus contributing to the formation of well-dispersed tiny Ni^0 nuclei that grow on the alumina surface at a limited extent to give small nanoparticles instead of few nuclei evolving as large metal particles, (ii) the occurrence of remaining nickel aluminate or related non stoichiometric nickel aluminate phases at the interface between the metal nanoparticle and alumina may improve the

stability of these highly dispersed Ni^0 nanoparticles by affording a particularly strong metal-support interaction, finally, (iii) this remaining $NiAl_2O_4$ is known to contain oxygen vacancies [49]. These species may therefore increase the CO_2 adsorption and thereby the catalytic activity. Furthermore, the active oxygen species generated by filling the oxygen vacancies of $NiAl_2O_4$ spinel by CO_2 may also provide a redox route to eliminate carbon species, responsible for the long-term stability and excellent resistance to coking and sintering of the MIL-53-derived catalysts in this study.

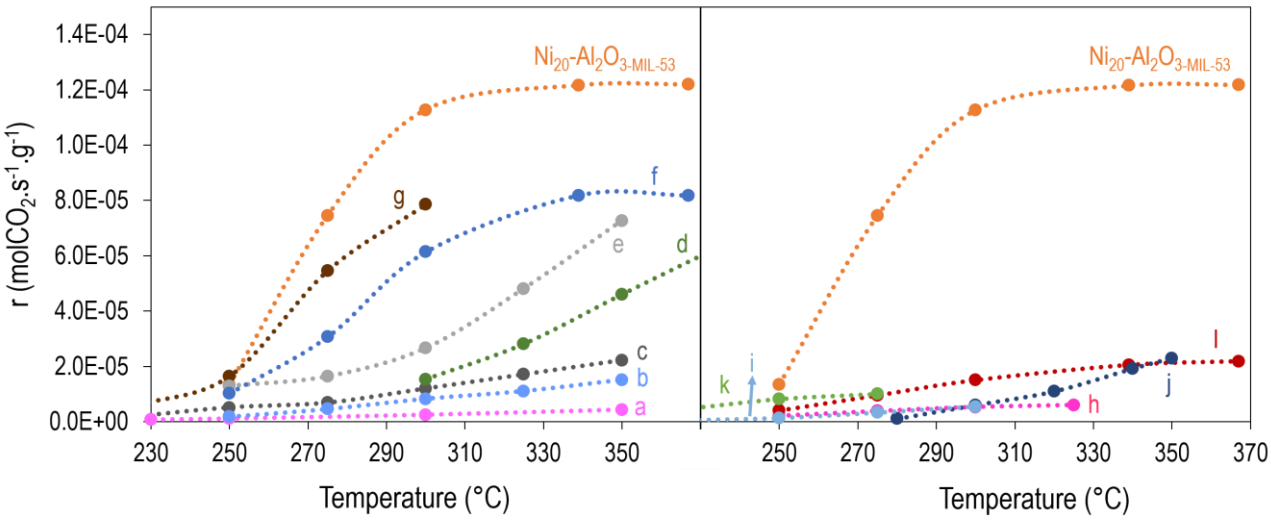

Figure 10: *Comparison in the 230-370°C temperature range of the average CO_2 reaction rates (in $mol_{CO2}.s^{-1}.g_{cat}^{-1}$) on Ni_{20}-$Al_2O_{3\text{-}MIL\text{-}53}$ (present work) and on catalysts of the literature detailed in Table S1: Ni-Al_2O_3 based catalysts Ni_{10}-$Al_2O_{3\ EISA}$ and Ni_{20}/Al_2O_3 (curves (a), (c)), other supported Ni-based catalysts (b) Ni_5/Sepiolite, (d) Ni_{10}/FDU, (e) Ni_{15}/MCM-41, (f) Ni_{30}/CNT, (g) Ni_9/ZrO_2, (h) Ni_{16}/Al_2O_3-ZrO_2-TiO_2-CeO_2, (i) Ni_{20}/SiC, (j) Ni_{20}/Bentonite, (k) Ni_{10}/CeO_2-ZrO_2, (l) Ni_{20}/KCC*

4. Conclusion

We described a novel approach for synthesizing active, selective and stable Ni-based alumina catalysts for CO_2 methanation based on the use of MIL-53(Al) as a highly porous pre-support. The impregnation of nickel precursors within the pores of this MOF enabled the homogeneous dispersion of Ni^{2+} in close proximity with an alumina source. After calcination and subsequent Ni^{2+} reduction into Ni^0, this strategy allowed the formation of well-dispersed and homogeneous Ni^0 nanoparticles embedded within γ-Al_2O_3 interwoven nanosheets. Interestingly, employing MIL-53(Al) as pre-support allowed to obtain a remarkably well-dispersed and active Ni^0 nanoparticles (size below 10 nm) even with Ni amount as high as 20 wt%. The performance of MIL-53(Al)-derived samples for the catalysis of the CO_2 methanation was shown to be higher than those of more conventional Ni-based catalysts, such as Ni^0 nanoparticles supported on γ-Al_2O_3 (a commercial catalyst from Evonik and a catalyst made by a one-pot EISA procedure) as well as on silica (Ni samples supported over a USY zeolite and a SBA-15

mesoporous silica). These better performances are mainly explained by the high dispersion of nickel nanoparticles within the MOF-derived catalysts and the formation after MOF calcination of nickel aluminate nanodomains that are presumed to play a positive role in the activity and stability of the catalyst. The best MOF-derived material (with Ni amount of 20 wt%; Ni_{20}-$Al_2O_{3\text{-MIL-53}}$) was also compared to other highly active methanation catalysts reported in literature. In all cases, MIL-53(Al)-derived materials led to superior performances, both in terms of CO_2 conversion and selectivity. Finally, these catalysts were shown to be remarkably stable even when submitted to time-on-stream as long as 20h.

Acknowledgments

The authors are grateful to the FP7 European program and related national organisms for SOL-CARE project funding (ERANETMED_ENERG-065, 2016-2019) and to the UOBRC for the BIRG 02/2016. M.C. Bacariza acknowledges *Fundação para a Ciência e Tecnologia* (FCT) for the financial support of the research group (UID/QUI/00100/2020). Sandra Casale (LRS, SU) is acknowledged for the recording of the electron microscopy images.

References

[1] H. Blanco, A. Faaij, A review at the role of storage in energy systems with a focus on Power to Gas and long-term storage, Renew. Sustain. Energy Rev. 81 (2018) 1049–1086. doi:10.1016/j.rser.2017.07.062.

[2] K. Ghaib, F.-Z. Ben-Fares, Power-to-Methane: A state-of-the-art review, Renew. Sustain. Energy Rev. 81 (2018) 433–446. doi:10.1016/j.rser.2017.08.004.

[3] J. Guilera, J. Ramon Morante, T. Andreu, Economic viability of SNG production from power and CO2, Energy Convers. Manag. 162 (2018) 218–224. doi:10.1016/j.enconman.2018.02.037.

[4] M. Sterner, Bioenergy and Renewable Power Methane In Integrated 100% Renewable Energy Systems: Limiting Global Warming By Transforming Energy Systems, kassel university press GmbH, 2009.

[5] P. Denholm, E. Ela, B. Kirby, M. Milligan, The Role of energy storage with renewable electricity generation, Publ. (2010) 1–61.

[6] T. Schaaf, J. Grünig, M.R. Schuster, T. Rothenfluh, A. Orth, Methanation of CO2 - storage of renewable energy in a gas distribution system, Energy. Sustain. Soc. 4 (2014) 2.

doi:10.1186/s13705-014-0029-1.

[7] C. Jia, J. Gao, Y. Dai, J. Zhang, Y. Yang, The thermodynamics analysis and experimental validation for complicated systems in CO2 hydrogenation process, J. Energy Chem. 25 (2016) 1027–1037. doi:10.1016/j.jechem.2016.10.003.

[8] W.J. Lee, C. Li, H. Prajitno, J. Yoo, J. Patel, Y. Yang, S. Lim, Recent trend in thermal catalytic low temperature CO2 methanation: A critical review, Catal. Today. (2020). doi:10.1016/j.cattod.2020.02.017.

[9] M. Younas, L. Loong Kong, M.J.K. Bashir, H. Nadeem, A. Shehzad, S. Sethupathi, Recent Advancements, Fundamental Challenges, and Opportunities in Catalytic Methanation of CO2, Energy and Fuels. 30 (2016) 8815–8831. doi:10.1021/acs.energyfuels.6b01723.

[10] C. Lv, L. Xu, M. Chen, Y. Cui, X. Wen, Y. Li, C.E. Wu, B. Yang, Z. Miao, X. Hu, Q. Shou, Recent Progresses in Constructing the Highly Efficient Ni Based Catalysts With Advanced Low-Temperature Activity Toward CO2 Methanation, Front. Chem. 8 (2020) 1–32. doi:10.3389/fchem.2020.00269.

[11] S. Tada, T. Shimizu, H. Kameyama, T. Haneda, R. Kikuchi, Ni/CeO2 catalysts with high CO2 methanation activity and high CH4 selectivity at low temperatures, Int. J. Hydrogen Energy. 37 (2012) 5527–5531. doi:10.1016/j.ijhydene.2011.12.122.

[12] P. Frontera, A. Macario, M. Ferraro, P. Antonucci, Supported Catalysts for CO2 Methanation: A Review, Catalysts. 7 (2017) 59. doi:10.3390/catal7020059.

[13] M. a. A. Aziz, A.A. Jalil, S. Triwahyono, A. Ahmad, CO2 methanation over heterogeneous catalysts: recent progress and future prospects, Green Chem. 17 (2015) 2647–2663. doi:10.1039/C5GC00119F.

[14] X. Su, J. Xu, B. Liang, H. Duan, B. Hou, Y. Huang, Catalytic carbon dioxide hydrogenation to methane: A review of recent studies, J. Energy Chem. 25 (2016) 553–565. doi:10.1016/j.jechem.2016.03.009.

[15] S. Saeidi, N.A.S. Amin, M.R. Rahimpour, Hydrogenation of CO2 to value-added products—A review and potential future developments, J. CO2 Util. 5 (2014) 66–81. doi:10.1016/j.jcou.2013.12.005.

[16] S. Rahmani, M. Rezaei, F. Meshkani, Preparation of promoted nickel catalysts supported on mesoporous nanocrystalline gamma alumina for carbon dioxide methanation reaction, J. Ind. Eng. Chem. 20 (2014) 4176–4182. doi:10.1016/j.jiec.2014.01.017.

[17] Q. Liu, S. Wang, G. Zhao, H. Yang, M. Yuan, X. An, H. Zhou, Y. Qiao, Y. Tian, CO2 methanation over ordered mesoporous NiRu-doped CaO-Al2O3 nanocomposites with enhanced catalytic performance, Int. J. Hydrogen Energy. 43 (2018) 239–250. doi:10.1016/j.ijhydene.2017.11.052.

[18] J. Gao, Q. Liu, F. Gu, B. Liu, Z. Zhong, F. Su, Recent advances in methanation catalysts for the production of synthetic natural gas, RSC Adv. 5 (2015) 22759–22776. doi:10.1039/c4ra16114a.

[19] L. Karam, M. Armandi, S. Casale, V. El Khoury, B. Bonelli, P. Massiani, N. El Hassan, Comprehensive study on the effect of magnesium loading over nickel-ordered mesoporous alumina for dry reforming of methane, Energy Convers. Manag. 225 (2020) 113470. doi:10.1016/j.enconman.2020.113470.

[20] L. Karam, M.C. Bacariza, J.M. Lopes, C. Henriques, P. Massiani, N. El Hassan, Assessing the potential of xNi-yMg-Al2O3 catalysts prepared by EISA-one-pot synthesis towards CO2 methanation: An overall study, Int. J. Hydrogen Energy. 45 (2020) 28626–28639. doi:10.1016/j.ijhydene.2020.07.170.

[21] M. Ding, R.W. Flaig, H.L. Jiang, O.M. Yaghi, Carbon capture and conversion using metal-organic frameworks and MOF-based materials, Chem. Soc. Rev. 48 (2019) 2783–2828. doi:10.1039/c8cs00829a.

[22] R. Lippi, S.C. Howard, H. Barron, C.D. Easton, I.C. Madsen, L.J. Waddington, C. Vogt, M.R. Hill, C.J. Sumby, C.J. Doonan, D.F. Kennedy, Highly active catalyst for CO2 methanation derived from a metal organic framework template, J. Mater. Chem. A. 5 (2017) 12990–12997. doi:10.1039/C7TA00958E.

[23] W. Li, A. Zhang, X. Jiang, C. Chen, Z. Liu, C. Song, X. Guo, Low Temperature CO2 Methanation: ZIF-67-Derived Co-Based Porous Carbon Catalysts with Controlled Crystal Morphology and Size, Acs Sustain. Chem. Eng. 5 (2017) 7824–7831. doi:10.1021/acssuschemeng.7b01306.

[24] L. Karam, J. Reboul, S. Casale, N. El Hassan, P. Massiani, Porous nickel-alumina derived from metal-organic framework (MIL-53): a new approach to achieve active and stable catalysts in methane dry reforming, ChemCatChem. 12 (2019) 373–385.

[25] L. Karam, J. Reboul, N. El Hassan, J. Nelayah, P. Massiani, Nanostructured nickel aluminate as a key intermediate for the production of highly dispersed and stable nickel nanoparticles

supported within mesoporous alumina for dry reforming of methane, Molecules. 24 (2019) 4107–4120. doi:10.3390/molecules24224107.

[26] V.I. Isaeva, A.L. Tarasov, V. V. Chernyshev, L.M. Kustov, Control of morphology and size of microporous framework MIL-53(Al) crystals by synthesis procedure, Mendeleev Commun. 25 (2015) 466–467. doi:10.1016/j.mencom.2015.11.023.

[27] M.C. Bacariza, I. Graça, J.M. Lopes, C. Henriques, Enhanced activity of CO2 hydrogenation to CH4 over Ni based zeolites through the optimization of the Si/Al ratio, Microporous Mesoporous Mater. 267 (2018) 9–19. doi:10.1016/j.micromeso.2018.03.010.

[28] M.C. Bacariza, I. Graça, J.M. Lopes, C. Henriques, Ni-Ce/Zeolites for CO2 Hydrogenation to CH4: Effect of the Metal Incorporation Order, ChemCatChem. 10 (2018) 2773–2781. doi:10.1002/cctc.201800204.

[29] L. Karam, N. El Hassan, Advantages of mesoporous silica based catalysts in methane reforming by CO 2 from kinetic perspective, J. Environ. Chem. Eng. 6 (2018) 4289–4297. doi:10.1016/j.jece.2018.06.031.

[30] M.W. Anderson, J. Klinowski, Zeolites treated with silicon tetrachloride vapour. Part 1.—Preparation and characterisation, J. Chem. Soc. Faraday Trans. 1 Phys. Chem. Condens. Phases. 82 (1986) 1449–1469. doi:10.1039/F19868201449.

[31] T. Remy, S.A. Peter, L. Van Tendeloo, S. Van der Perre, Y. Lorgouilloux, C.E.A. Kirschhock, J.A. Martens, Y. Xiong, G. V. Baron, J.F.M. Denayer, Adsorption and separation of CO2 on KFI zeolites: effect of cation type and Si/Al ratio on equilibrium and kinetic properties, Langmuir ACS J. Surfaces Colloids. 29 (2013) 4998–5012. doi:10.1021/la400352r.

[32] M.C. Bacariza, M. Maleval, I. Graça, J.M. Lopes, C. Henriques, Power-to-methane over Ni/zeolites: Influence of the framework type, Microporous Mesoporous Mater. 274 (2019) 102–112. doi:10.1016/j.micromeso.2018.07.037.

[33] W.J. Jang, H.M. Kim, J.O. Shim, S.Y. Yoo, K.W. Jeon, H.S. Na, Y.L. Lee, D.W. Jeong, J.W. Bae, I.W. Nah, H.S. Roh, Key properties of Ni-MgO-CeO2, Ni-MgO-ZrO2, and Ni-MgO-Ce(1-x)Zr(x)O2 catalysts for the reforming of methane with carbon dioxide, Green Chem. 20 (2018) 1621–1633. doi:10.1039/c7gc03605a.

[34] M.K. Nazemi, S. Sheibani, F. Rashchi, V.M. Gonzalez-Delacruz, A. Caballero, Preparation of nanostructured nickel aluminate spinel powder from spent NiO/Al2O3 catalyst by mechano-chemical synthesis, Adv. Powder Technol. 23 (2012) 833–838. doi:10.1016/j.apt.2011.11.004.

[35] M. Shah, S. Das, A.K. Nayak, P. Mondal, A. Bordoloi, Smart designing of metal-support interface for imperishable dry reforming catalyst, Appl. Catal. A Gen. 556 (2018) 137–154. doi:10.1016/j.apcata.2018.01.007.

[36] C.M. Mfoumou, S. Mignard, T. Belin, The preferential adsorption sites of H2O on adsorption sites of CO2 at low temperature onto NaX and BaX zeolites, Adsorpt. Sci. Technol. (2018) 1–14. doi:10.1177/0263617418762494.

[37] M.C. Bacariza, M. Biset-Peiró, I. Graça, J. Guilera, J. Morante, J.M. Lopes, T. Andreu, C. Henriques, DBD plasma-assisted CO2 methanation using zeolite-based catalysts: Structure composition-reactivity approach and effect of Ce as promoter, J. CO2 Util. 26 (2018) 202–211. doi:10.1016/j.jcou.2018.05.013.

[38] A. Cárdenas-Arenas, A. Quindimil, A. Davó-Quiñonero, E. Bailón-García, D. Lozano-Castelló, U. De-La-Torre, B. Pereda-Ayo, J.A. González-Marcos, J.R. González-Velasco, A. Bueno-López, Isotopic and in situ DRIFTS study of the CO2 methanation mechanism using Ni/CeO2 and Ni/Al2O3 catalysts, Appl. Catal. B Environ. 265 (2020). doi:10.1016/j.apcatb.2019.118538.

[39] A. Westermann, B. Azambre, M.C. Bacariza, I. Graça, M.F. Ribeiro, J.M. Lopes, C. Henriques, Insight into CO2 methanation mechanism over NiUSY zeolites: An operando IR study, Appl. Catal. B Environ. 174–175 (2015) 120–125. doi:10.1016/j.apcatb.2015.02.026.

[40] A. Lechkar, A. Barroso Bogeat, G. Blanco, J.M. Pintado, M. Soussi el Begrani, Methanation of carbon dioxide over ceria-praseodymia promoted Ni-alumina catalysts. Influence of metal loading, promoter composition and alumina modifier, Fuel. 234 (2018) 1401–1413. doi:10.1016/j.fuel.2018.07.157.

[41] L. Karam, S. Casale, H. El Zakhem, N. El Hassan, Tuning the properties of nickel nanoparticles inside SBA-15 mesopores for enhanced stability in methane reforming, J. CO2 Util. 17 (2017) 119–124. doi:10.1016/j.jcou.2016.12.002.

[42] I. Graça, L. V. González, M.C. Bacariza, A. Fernandes, C. Henriques, J.M. Lopes, M.F. Ribeiro, CO2 hydrogenation into CH4 on NiHNaUSY zeolites, Appl. Catal. B Environ. 147 (2014) 101–110. doi:10.1016/j.apcatb.2013.08.010.

[43] J.H. Park, S. Yeo, T.S. Chang, Effect of supports on the performance of Co-based catalysts in methane dry reforming, J. CO2 Util. 26 (2018) 465–475. doi:10.1016/j.jcou.2018.06.002.

[44] W. Zhen, B. Li, G. Lu, J. Ma, Enhancing catalytic activity and stability for CO2 methanation

on Ni@MOF-5 via control of active species dispersion, Chem. Commun. 51 (2015) 1728–1731. doi:10.1039/C4CC08733J.

[45] A. Cárdenas-Arenas, A. Quindimil, A. Davó-Quiñonero, E. Bailón-García, D. Lozano-Castelló, U. De-La-Torre, B. Pereda-Ayo, J.A. González-Marcos, J.R. González-Velasco, A. Bueno-López, Isotopic and in situ DRIFTS study of the CO2 methanation mechanism using Ni/CeO2 and Ni/Al2O3 catalysts, Appl. Catal. B Environ. 265 (2020) 118538. doi:10.1016/j.apcatb.2019.118538.

[46] J. Yang Lim, J. McGregor, A.J. Sederman, J.S. Dennis, Kinetic studies of CO2 methanation over a Ni/γ-Al2O3 catalyst using a batch reactor, Chem. Eng. Sci. 141 (2016) 28–45. doi:10.1016/j.ces.2015.10.026.

[47] C. Vogt, M. Monai, E.B. Sterk, J. Palle, A.E.M. Melcherts, B. Zijlstra, E. Groeneveld, P.H. Berben, J.M. Boereboom, E.J.M. Hensen, F. Meirer, I.A.W. Filot, B.M. Weckhuysen, Understanding carbon dioxide activation and carbon–carbon coupling over nickel, Nat. Commun. 10 (2019) 1–10. doi:10.1038/s41467-019-12858-3.

[48] M.C. Bacariza, I. Graça, S.S. Bebiano, J.M. Lopes, C. Henriques, Micro- and mesoporous supports for CO2 methanation catalysts: A comparison between SBA-15, MCM-41 and USY zeolite, Chem. Eng. Sci. 175 (2018) 72–83. doi:10.1016/j.ces.2017.09.027.

[49] S. Zhang, M. Ying, J. Yu, W. Zhan, L. Wang, Y. Guo, Y. Guo, NixAl1O2-δ mesoporous catalysts for dry reforming of methane: The special role of NiAl2O4 spinel phase and its reaction mechanism, Appl. Catal. B Environ. 291 (2021) 120074. doi:10.1016/j.apcatb.2021.120074.